FROM QUANTUM HALL TO QUANTUM FARADAY:

DESIGN AND ANALYSIS OF AN EXPERIMENT

By

TALIA MARTZ-OBERLANDER

A thesis submitted in partial fulfillment of
the requirements for the degree of

MASTER OF SCIENCE

MCGILL UNIVERSITY
Department of Physics

NOVEMBER 2020

בס"ד

ACKNOWLEDGMENTS

Physics research is not done in a perfect box under vacuum by a lone actor and I would like to acknowledge those who have supported this work. First and foremost I would like to thank my supervisor, Prof. Gervais, who has not only made this work possible through the creation and leadership of G^2 Lab, but has offered motivation, opportunities for growth, and intellectual challenge beyond measure. Thank you for bringing me aboard. Thank you also to faculty member Prof. Szkopek for highly insightful discussions and invaluable contributions to this work.

Thank you to my colleagues and collaborators for their support and enrichment: Anthony, Eli, Fred, Matei, Oulin, Sujatha and particularly Vishnu at Université de Sherbrooke, as well as undergraduate researchers, Chloé and Zach. A special thank you to Robert, Richard, and John for your technical support and great spirits. Thank you to Zhao, Hélène, and their respective teams at McGill NanoFab and at École Polytechnique for teaching me various fabrication techniques. I would also like to thank the support staff in the Department of Physics for all their work and all those who strive for a more habitable workplace.

I would like to acknowledge that this work is conducted on the unceded lands of the Kanien'kehá:ka, and as a settler here I humbly fight for land back. Thank you to my partner, Naftoli, for picking up the loose ends and convincing me to believe in myself. I stand upon the shoulders of giants: to my family and ancestors and other relations I thrive thanks to your efforts to survive in the face of adversity. Thank you for the gift of being able to pursue my curiosities.

ABSTRACT

The discovery of the quantum Hall effect (QHE) in the latter twentieth century sparked a revolution for condensed matter physics and provided a new universal standard for resistance in metrology. Probing low temperature quantum behaviour of two-dimensional electron gases (2DEGs) in various semiconductor materials changed our understanding of particle interactions in low-dimensions. Beyond direct current transport measurements, numerous experimental environments including optical measurements, like Faraday rotation, continue to provide insights into our quantum world. Both Hall and Faraday effects arise in the presence of a magnetic field from the Lorentz force on electrons in the 2DEG. Both effects were classically defined in the 1800s and provided great technological advances for electronics and communication. Faraday rotation manifests itself in a wide range of physical settings from radio waves through interstellar gases to X-ray transmission in metals. Where the quantum Hall effect and derivative research has opened up pathways for quantum computing, quantized Faraday rotation could support twenty-first century non-reciprocal radio or microwave control. We have found that high electron mobility in 2DEGs enables giant single-pass rotation of $\theta_F^{\max} \simeq 45^o \simeq (0.8 \text{ rad})$ and robust integer quantum Hall states in the high magnetic field range. This thesis presents background and experiments in the QHE as well as quantized Faraday rotation. Measurements for both phenomena are presented and a design for future studies of quantized Faraday rotation is presented. Future research goals of quantized Faraday measurements include room temperature measurements in high spin-orbit materials and observation of fractional quantum Faraday effects at low temperatures.

ABRÉGÉ

La découverte de l'effet Hall quantique (EHQ) à la fin du vingtième siècle a déclenché une révolution pour la physique de matière condensée et a offert un nouveau standard universel pour la résistance en métrologie. Sonder le comportement quantique à basse température de gaz d'électrons bidimensionnels (GEBDs) dans divers matériaux semi-conducteurs a changé notre compréhension de l'intéraction des particules en basses dimensions. Au-delà des mesures directes de transport de courant, plusieurs environnements expérimentaux, incluant les mesures optiques comme la rotation Faraday, continuent d'offrir une perspective dans le monde quantique. Les effets Hall et Faraday se révèlent en la présence d'un champ magnétique et sont issus de la force Lorentz sur des électrons dans le GEBD. Ces deux effets ont été définis dans les années 1800, et ont fourni de grandes avancées pour l'électronique et la communication. La rotation Faraday se manifeste dans une grande gamme de cadres physiques, commes les ondes radio à travers des gaz interstellaires ou la transmissions de rayon-X dans les métaux. Alors que l'effet Hall quantique entier et ses recherches dérivées ont ouvert la voie pour le calculateur quantique, la rotation Faraday quantifiée pourrait faire avancer la radio non-réciproque ou le contrôle des signaux micro-ondes du 21e siécle. Nous avons decouvert que la haute mobilité des électrons en GEBDs permet des passages uniques de rotations de $\theta_F^{\max} \simeq 45^o \simeq$ (0.8 rad) et des états Hall quantiques entiers dans la gamme de hauts champs magnétiques. Cette mémoire présente le contexte et les expérimentations dans l'EHQ, ainsi que la rotation Faraday quantifiée. Des mesures pour ces deux phénomènes ainsi qu'un design pour de futures études de la rotation Faraday quantifiée sont présentés.

Les objectifs prochains de cette recherche incluent des mesures sur des matériaux à haut couplage spin-orbite, et l'observation de l'effet Faraday quantatique fractionnaire à basses températures.

CONTRIBUTIONS

I was responsible for the work presented in this thesis for measurements of flip-chip devices, Van der Pauw device fabrication, certain analysis of Faraday rotation, and design of future experiments. Certain new measurements, such as charge carrier density, mobility, and quantum lifetime measurements for our GaAs wafers were planned for Spring 2020 but had to be omitted from the thesis due to the closure of the laboratory for the COVID-19 pandemic (Section 1.2.1 and 1.2.2).

The original parts of the flip-chip devices I measured were created or designed by past students (e.g. G10 sample holder design and electronic gating fabrication by Prof. Bennaceur, Samuel Gaucher, and Simon Bernier). I took all components individually, preparing them and in some cases repairing them using clean room machinery for assembly and conducted all measurements mentioned in Section 1.3.

The measurements of quantized Faraday rotation presented in Chapter 2 were conducted by Vishnunarayanan Suresh with Prof. Reulet at UdS in collaboration with the groups of Prof.'s Szkopek and Gervais at McGill University (see citation for full author list). In parallel with other authors, I conducted the analysis of this dataset for the Landau indexing, charge carrier density, and Drude model fit. I also provided certain figures for the paper.

I designed the future Faraday experiments at McGill on the newly commissioned Oxford Triton refrigerator under the guidance of Prof. Gervais, Prof. Szkopek, and Richard Talbot.

TABLE OF CONTENTS

Page

ACKNOWLEDGMENTS ii

ABSTRACT iii

ABRÉGÉ iv

CONTRIBUTIONS vi

1 Quantum Hall Effect 1
- 1.1 Background to the quantum Hall effect 2
  - 1.1.1 Landau level physics 2
  - 1.1.2 Hall effect 4
  - 1.1.3 Integer quantum Hall effect 6
  - 1.1.4 Fractional quantum Hall effect 8
- 1.2 Transport measurements in 2D electron gases 9
  - 1.2.1 Mobility and charge carrier density from Van der Pauw measurements 12
  - 1.2.2 Dingle plots and quantum lifetime measurements 14
- 1.3 Gated devices for Hall state interferometry 16
  - 1.3.1 Interferometry 16
  - 1.3.2 Flip-chip device 16
  - 1.3.3 Postmortem analysis 21

2 Quantum Faraday Effect 25
- 2.1 Derivation of Faraday angle of rotation in a 2DEG 26
- 2.2 Previous experimental works 28
  - 2.2.1 Microwave experiments (GHz) 28
  - 2.2.2 Optical Experiments (THz) 30

2.3 McGill-Sherbrooke collaborative work . . . 31
2.3.1 Experimental setup . . . 31
2.3.2 Experimental data . . . 33
2.3.3 Electromagnetic confinement . . . 34
2.3.4 Classical Drude model . . . 34
2.3.5 Integer quantum Faraday effect . . . 35
2.3.6 Extraction of α* . . . 38

3 Design of a Faraday experiment for a tri-axis vector magnet cryostat at McGill . . . 41
3.1 Microwave experiment design . . . 42
3.1.1 Considerations of operating frequencies . . . 42
3.1.2 Wafer configuration . . . 44
3.1.3 Waveguide design . . . 46
3.2 Laboratory configuration . . . 49
3.2.1 VNA Data Configuration . . . 49
3.2.2 Experimental circuit . . . 49

4 Conclusion . . . 52
4.1 Future experiments at room temperature . . . 53
4.1.1 High mobility materials . . . 53
4.1.2 High spin-orbit materials . . . 54
4.2 Fractional quantum Faraday effect . . . 54

REFERENCES . . . 59

APPENDIX

A Wafer cleaving process . . . 61

B Wafer cleaning recipe . . . 63

C McGill Faraday experiment waveguide parts . . . 64

D Sample wafer growth sheet . . . 65

Chapter One

Quantum Hall Effect

The discovery of the quantum Hall effect (QHE) in the later twentieth century has blossomed into a popular new field of condensed matter physics. With deep implications for low-dimensional physics, semiconductor physics, quantum computing, and metrology, QHE research has been marked by unexpected new experimental discoveries. Klaus von Klitzing, in his Nobel prize speech of 1985 reminds us that, while semiconductors are electronically complicated materials, they allow us to measure and comprehend fundamental quantized figures of the universe [1]. While the states of integer QHE (IQHE) are populated by freely moving electrons, the states of the fractional QHE (FQHE) are thought to be governed by electron interactions. Perhaps the most mysterious aspect of the QHE is the apparent formation of the particles known as composite fermions (CFs), which occupy fractional filling states. In certain fractional states, such as $\nu = 5/2$, these CFs defy both types of particle statistics, bosonic and fermionic, that modern physics allows. Such states have been theorised and measured experimentally, however clarity on their nature is still lacking. Understanding the basis for such phenomena rests upon future investigations and innovative experimental techniques.

In this chapter, I provide an overview of groundbreaking discoveries and foundational concepts of the QHE as the basis for our understanding of quantized Faraday rotation, found to be an optical analog of the QHE. I provide a brief experimental and theoretical background followed by a review of experiments I conducted using specialized flip-chip devices for novel QHE gating.

1.1 Background to the quantum Hall effect

1.1.1 Landau level physics

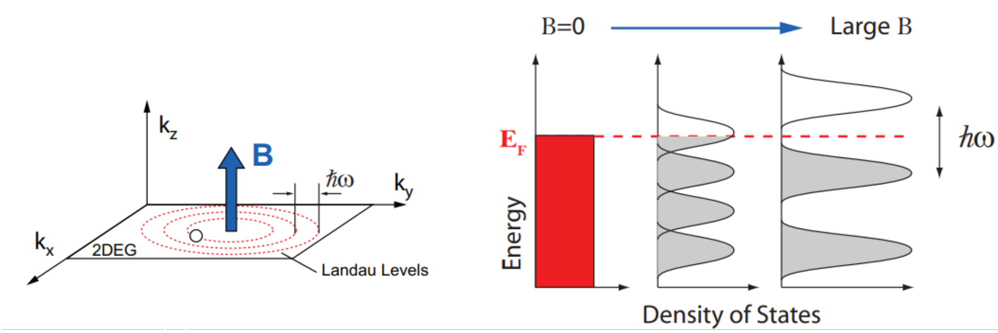

Figure 1.1 Formation of Landau levels in the QHE. Left: In the magnetic field B electrons are confined to cyclotron orbit with each energy level known as a Landau Level (LL) separated by width $\hbar\omega_c$ shown here in energy k space, **Right:** From the view of density of states (DOS, commonly labeled g), increasing B causes increasing separation of energy levels enabling the measurement of distinct LLs. From Cory Dean's PhD thesis [2].

Both the IQHE and FQHE states are well described with Landau levels (LLs) in a two-dimensional (2D) system. Landau levels in the QHE are degenerate energy states directly proportional to magnetic field strength. In an ideal, disorder-free system in the presence of a magnetic field B, the electron energy states collapse into quantized circular orbits in the plane transverse to the B field. These energy states are separated by a well-defined energy gap $\hbar\omega_c$, where ω_c is the cyclotron frequency. In 3D, electrons can inhabit any state on the quasi-continuous energy spectrum along the z-axis. However, in the 2D limit at low temperatures, the LLs represent the only energy levels, confined to the x, y plane the electrons can occupy due to such a large energy gap.

To better understand the integer quantum Hall effect (IQHE) we can begin with the solution for the Schroedinger equation for an electron confined to 2D,

$$E_N = (N + 1/2)w_c \tag{1.1}$$

where $N = 0, 1, 2, ...$ refers to each Landau level and w_c is given by

$$w_c = \frac{eB}{m^*} \tag{1.2}$$

with m^* the effective mass of the electron. For the GaAs semiconductor wafers used for the experiments described in this thesis, $m^* = 0.067m_e$. In the absence of a magnetic field, the density of states (DOS) in 2D is constant as a function of energy. However with a magnetic field and in the ideal case, the density of states collapses onto a series of highly degenerate, separated δ-functions corresponding to the LLs. In real samples, the δ-functions are broadened due to disorder scattering. The width of this broadening is referred to as Γ and is further discussed in an experimental context in Section 1.2. There are a number of energy states within each LL given by the magnetic field strength defining the LL degeneracy:

$$n_B = \frac{eB}{h}. \tag{1.3}$$

This formula for the number of states does not include spin degeneracy, which would contribute an additional factor of two. As the magnetic field is increased, as shown in Fig. 1.1, the size of orbits in k-space increases and so does the available space for more electrons as in Eq. 1.3. At very low temperatures, electrons fill the lowest available energy states. At low temperatures and low magnetic fields, a large number of LLs will in general be filled. As the magnetic field is increased the LL degeneracy increases and more electrons inhabit the increased number of states in the lowest LLs, containing both integer and fractional filling factors as discussed below.

1.1.2 Hall effect

The Hall effect describes the behaviour of charged particles in a conductor in the presence of an applied magnetic field. Specifically, in 1879 Edwin Hall measured a voltage transverse to the current passing through metal foil in the presence of a magnetic field at room temperature [3].

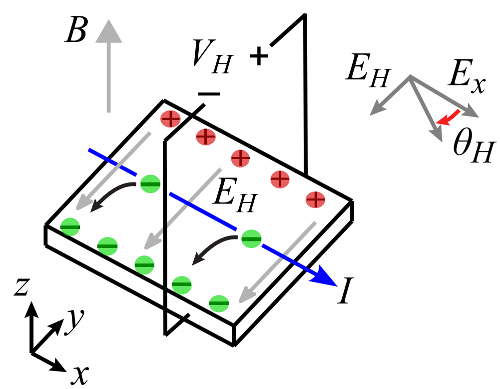

Figure 1.2 Cartoon of the Hall effect in a wafer. A current I flows through a conductive material in the presence of a perpendicular magnetic field B causing electrons to drift to the side. This creates a transverse voltage V_H [4].

This observation is explained by the Lorentz force, which states that a charged particle moving in the presence a magnetic field experiences a force given by

$$\mathbf{F}_B = -e(\mathbf{v} \times \mathbf{B}), \tag{1.4}$$

where $\mathbf{F}_B$ is the component of the Lorentz force driven by the magnetic field, e is electron charge, $\mathbf{v}$ is the electron velocity and $\mathbf{B}$ is the magnetic field vector. In the Hall effect, electrons drift transversely to the original current flow causing an accumulation of charge and a voltage potential across the sides of the sample. This charge imbalance creates an electric field with its own force

$$F_e = \frac{eV_H}{w}, \tag{1.5}$$

where w is the sample width and V_H is the transverse voltage known as the Hall voltage. As the Hall voltage increases, so does the electrostatic force and equilibrium is then reached between the two, Eq. 1.4 and 1.5, yielding

$$\frac{eV_H}{w} = ev_d B, \tag{1.6}$$

where v_d is the electron drift velocity. To further understand the Hall effect, we begin by considering classical current flowing through this sample,

$$I = Nev_d A \tag{1.7}$$

where N is the electron density and $A = wd$ is the area within which the electrons flow defined by the sample width w and thickness d. Rearranging Eq. 1.7 for drift velocity substituted into Eq. 1.6 provides the relationship between Hall voltage, current, and magnetic field,

$$V_H = \frac{IBw}{eNA}. \tag{1.8}$$

If we consider a thin sample where $d \ll w$, the electron density is well-defined by planar density in the 2D limit and we can utilize $n = Nd$. Canceling out terms, the Hall voltage becomes

$$V_H = \frac{IB}{ne}. \tag{1.9}$$

Since longitudinal electron transport in the direction of current flow is unaffected by the magnetic field B, the longitudinal resistance R_{xx} follows Ohms law relation,

$$R_{xx} = \frac{V_{xx}}{I}. \tag{1.10}$$

Recalling the equilibrium from Lorentz (Eq. 1.4) and electrostatic force (Eq. 1.5), we readily obtain that there is no current flow in the transverse direction in the sample, only voltage. By convention, we define the resistance relation from V_H, where $R_H = V_H/I$, to be

$$R_H = \frac{B}{ne}. \tag{1.11}$$

It is important to note that Hall resistance depends solely on the strength of the magnetic field and electron density and that no physical parameters of the sample, such as size, are involved.

1.1.3 Integer quantum Hall effect

The quantized states of the Hall effect were first observed in 1980, when von Klitzing, Dorda, Pepper, and colleagues demonstrated quantization in the Hall resistance of a 2D electron system at high magnetic fields [5]. The plot of R_H contained strong plateaus, whereas resistance follows the classical behaviour and is linear in B. Additionally,the spacing between plateaus followed a pattern of fundamental units, h/e^2, with h the Planck constant and e the electron charge. This discovery later led to the adoption of the latest universalised measure of resistance [6].

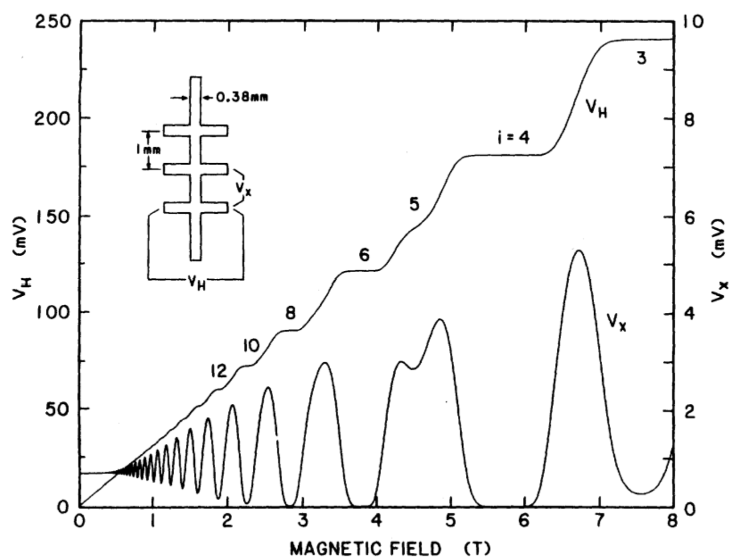

Figure 1.3 Quantized plateaus in $V_{xx} = IR_{xx}$ and $V_H = IR_H$ as a function of B field in GaAs at 1.2K. R_H increases linearly with magnetic field, however it is also striked with quantized at multiples of h/e^2 seen as plateaus. At the same B values, the minima in R_{xx} occur when the Fermi energy lies between two energy levels, such that the density of states at the Fermi energy is a minimum. Figure from Cage *et al.* [7]

The quantum Hall effect is observed when the Fermi energy lies in the energy gap of a group of many electrons with two-dimensional freedom, often in an environment called a two-dimensional electron gas (2DEG), and if the thermal energy is low enough to prevent excitations across the gap. In the quantum Hall regime, plateaus in R_H appear at well-defined values of B. For the IQHE, transverse resistance follows integer indexing denoted by $i = 2, 3, 4...$, where

$$R_H = \frac{h}{ie^2} \tag{1.12}$$

where h is Planck's constant and i is the index for integer filling.

1.1.4 Fractional quantum Hall effect

Indexing of states in the fractional quantum Hall effect (FQHE) can be conceptualized as the ratio between charge carriers (electrons) and magnetic flux quanta. The fractional filling factor is denoted as $\nu = \frac{n}{n_B}$, where n is the electron density and $n_B = B/\Phi_o$, where the flux quantum $\Phi_o = h/e$. To explain the fractional filling protocol, we can take the example of the fractional states in the lowest LL. Here $n = 1$ and spin branches are counted as $n_B = 2, 3...$ (*e.g.* $v = \frac{1}{3}$). Compared to the i index system from the IQHE, ν is the more general form of i and ν can be written as i when n is a multiple of n_B. Interestingly, in all cases where the quantum Hall states are well formed, (*i.e.* $\sigma_H = h/\nu e^2$) be it integer or fractional, concomitantly R_{xx} vanishes.

Dan Tsui and colleagues observed that exact quantization in the Hall resistance occurs together with a zero value in the magnetoresistance in 1982 [8]. This is the fundamental characteristic of the QHE. Further, conflicting with early theories of the QHE, Tsui and Stormer, and Gossard observed fractional filling within the lowest Landau level with a 1/3 filling factor. Different filling fractions display different physical behaviours, including non-Abelian statistics [9]. As it is not directly related to measurements conducted in this work, the FQHE only bears mention here. Many interesting studies have been conducted in the past forty years and further reading can be found in the following works [**Girvin1990**, 10–13].

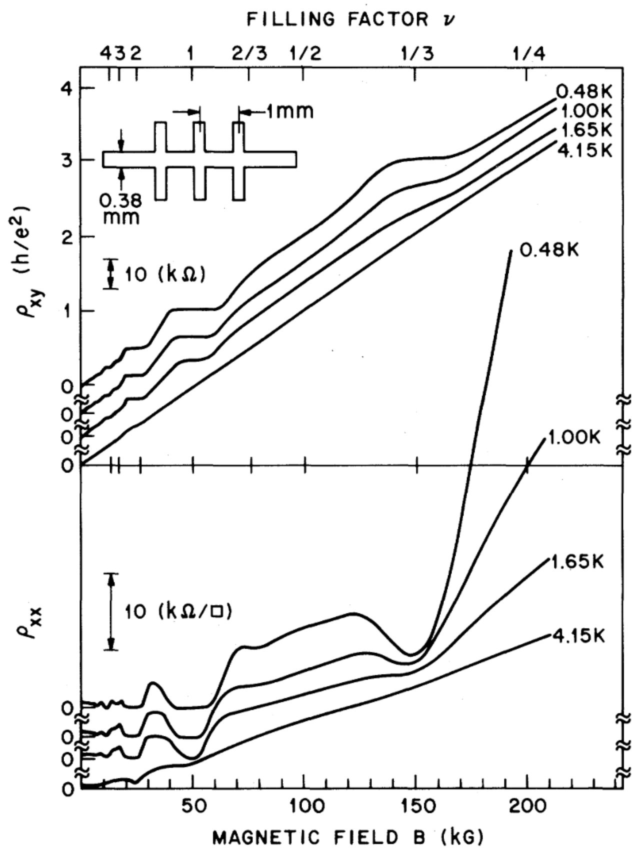

Figure 1.4 First observation of a fractional quantum Hall state. Integer states as well as fractional filling factors ν within first LL are present. At low temperatures, ρ_{xx} vanishes at the plateaus in ρ_{xy}. Image from Tsui *et al.* [8].

1.2 Transport measurements in 2D electron gases

We have seen that 2DEGs with characteristically high-mobility have played a foundational role in QHE experiments over the past four decades. This section explores the qualities of 2DEGs and certain measurements of their characteristics used in quantum Hall experiments.

2DEGs are hosted inside a heterogeneous semiconductor, most commonly created using molecular beam epitaxy (MBE) and modulation doping. The wafers are created by spraying GaAs and AlGaAs molecules on to a GaAs substrate inside an ultra-high-vacuum chamber (see sample growth sheet in Appendix D). Modulation doping involves adding silicon atoms

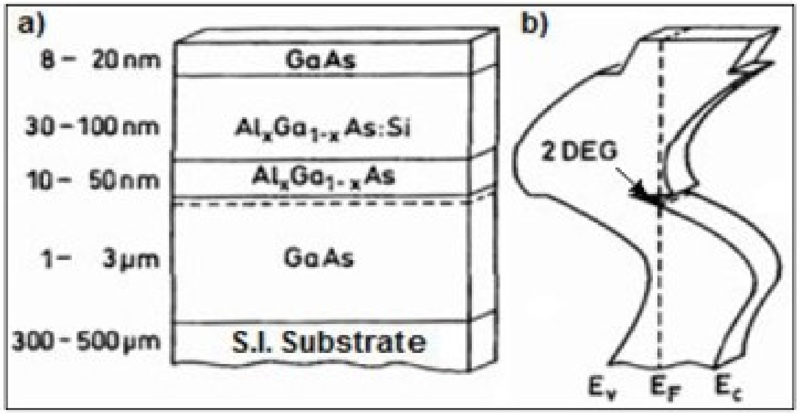

Figure 1.5 Two dimensional electron gas (2DEG). a) Spacial diagram of a GaAs heterostructure. **b)** Sketch of energy levels within the wafer levels with 2DEG in the quantum well seen dipping below the Fermi energy E_F. Image from Rodriquez *et al.* [14].

during the epitaxy process such that the electrons from silicon atoms in the AlGaAs layers will migrate to the GaAs regions, which possess lower-energy conduction bands than the AlGaAs layers [15]. The resulting effect provides delocalized electrons from the silicon nuclei within the wafer's crystal structures. The layers of deposition for low-temperature experiments are chosen such that, once cooled, the electrons will "sink" into a 2D quantum well with high lateral mobility in xy and a high potential barrier in z, the height of the wafer layers; this forms the 2DEG. Wafers are often 2" or 4" circles with width $d \simeq 0.5$ mm with the quantum well 30 nm thick set 100 nm below the wafer surface. To obtain the energetic confinement for low-dimensions in semiconductors, the average thermal energy of the electrons must be lower than the excitation energy along the confined direction, $\Delta \geq k_B T$ [16]. To this end, experiments are often conducted in refrigerators with temperatures in the tens of milliKelvins (mK).

As presented in Section 1.1, the QHE possesses geometry-free relations. To obtain measurements without experimentally imposed geometric constraints, it is common to measure resistivity ρ and conductivity σ, the geometrically-independent analogues of resistance R and conductance G, respectively. In experiments, utilising certain simple shapes, such as squares, offers ease of translation from measured conductance to conductivity, where $\sigma = G/L = G\frac{A}{W}$ and $A = WL$ is wafer area, width, and length (Fig. 1.6). An example of this can be seen in Fig. 1.7, where Van der Pauw wafers allow for the elimination of geometric factors of resistance. It also provides the ability to take multiple comparable cross-sample measurements simultaneously to eliminate wire resistance.

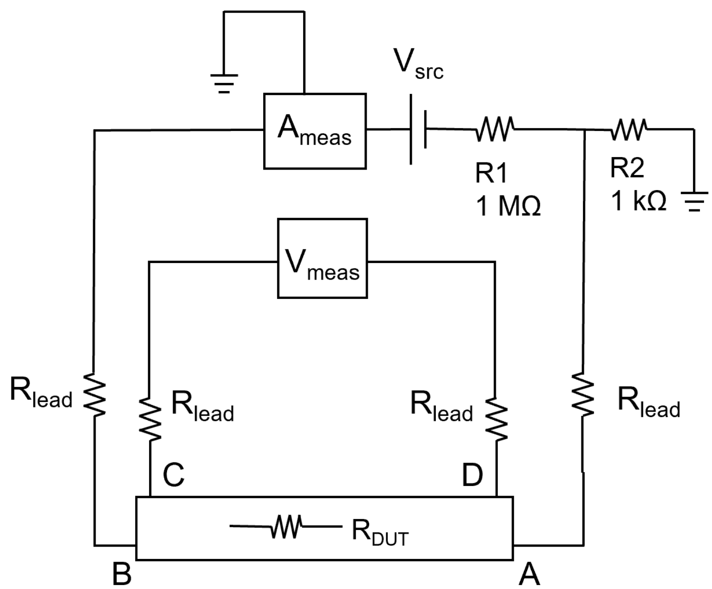

Figure 1.6 Four-point conductance measurements of a Hall bar device. A,B,C, and D are ohmic contacts on the GaAs semiconductor, where at A: voltage is applied from a lock-in amplifier to R1 such that a current is supplied to contact A after being divided using R2. Current is measured from contact B after passing through the device under test (DUT). Voltage is measured by taking V_C-V_D. $V_{src} =$ 0.1 V such that $I_{src} = \frac{V_{src}}{R1} = 100$nA.

Further, it can be convenient to measure conductivity rather than resistivity due to the values of current and voltage used in transport measurements. For example, if resistivity is too small for the experimental setup, conductivity will be large enough to measure. Additionally, some studies rely on conductivity measured via signal transmission (discussed in Sections 2.2.2, 2.2.3). Conductivity is defined from current and electric field in a medium as $J = \sigma E$; however, in the presence of a magnetic field and transverse voltage, conductivity is anisotropic and is best expressed by the conductivity tensor

$$\hat{\sigma} = \begin{pmatrix} \sigma_{xx} & \sigma_H \\ -\sigma_H & \sigma_{yy} \end{pmatrix}. \tag{1.13}$$

1.2.1 Mobility and charge carrier density from Van der Pauw measurements

As mentioned in Section 1.1, having highly mobile electrons is necessary for observing quantum Hall states. Here, we briefly discuss mobility in the QHE as well as the density of charge carriers. Mobility is defined as the ratio of the drift velocity to the electric field [17],

$$\mu \equiv \left| \frac{V_d}{E} \right| = \frac{|e|\tau_m}{m} \tag{1.14}$$

where v_d is drift velocity, E is electric field, e is electron charge, m is momentum, and τ_m is momentum relaxation time, which will . Note that mobility is non-directional. The ideal system is often referred to as a "pure" heterostructure semiconductor, in reference to high drift velocity and long relaxation time or low scattering. The best mobilities in 2DEGs in physics today are $\sim 35 \times 10^6$ cm^{2}V^{-1}s^{-1} [18].

We can extract mobility experimentally from transport measurements. This is very useful for experimentalists because one can use a small piece of a semiconductor wafer to measure mobility and determine whether that heterostructure is a good candidate for hosting quantum Hall states before fabricating a more advanced device out of the wafer. Many 4"

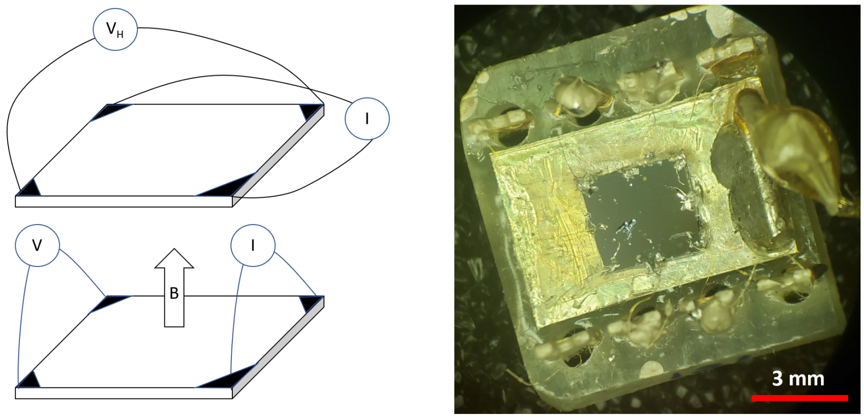

Figure 1.7 Van der Pauw (VdP) geometric device for finding the density and mobility of a semiconducting wafer. Left: VdP geometry makes use of square symmetries to measure resistance or conductance in various directions across a small piece of wafer. Since width and length are the same in VdP geometry, one can compare various configurations for current and voltage measurements supporting geometry-free density and mobility measurements. **Right:** VdP device with thermalizing platform (silver) and 3 $\times$ 3 mm GaAs semiconductor (black) placed in the center. Current and voltage are transmitted and measured using contacts on the wafer's sides or corners using the indium-annealed wires, seen around the edges.

wafers are heterogeneous and as such it is possible to find significant differences in density and mobility between various millimeter-scale pieces taken from the disk. To extract mobility from transport measurements, we first extract charge carrier density, n. This is achieved by taking the linear fit of the integer Landau levels from σ_H versus magnetic field in the high B regime by rearranging Eq. (1.9), such that

$$n = \frac{IB}{eV_H}. \tag{1.15}$$

Once we obtain n, the mobility can be calculated from

$$\sigma = \mu \; n \; e. \tag{1.16}$$

This formula is applied to a fit of the low-field resistance on either side of $B = 0$. When 4-point contact measurements are used, this method also accounts for the contact resistance in one's device wiring. Unfortunately, I have not been able to measure my Van der Pauw devices due to laboratory closures for COVID-19, and so I am unable to demonstrate this technique. However, a full description can be found in Benjamin Schmidt's PhD thesis [19].

1.2.2 Dingle plots and quantum lifetime measurements

Conductivity (or resistivity) can be used to determine the Landau level broadening $\Gamma = \hbar/2\tau_q$, where τ_q is the so-called quantum lifetime. Quantum lifetime is a measure of scattering of charge carriers and depends on material properties. In the low magnetic field regime ($B < 1$ T), ρ_{xx} oscillates, known as Shubnikov de Haas (SdH) oscillations, at some frequency from which we can determine Γ or τ_q from its amplitude. The dependence of quantum lifetime on the magnetic field depends on the form that the oscillations follow, namely either

$$\frac{\Delta\rho_{xx}}{\rho_{xx}} = A \exp\left(\frac{-\pi}{w_c\tau_q}\right), \text{ for Lorentzian broadening or,} \tag{1.17}$$

$$\frac{\Delta\rho_{xx}}{\rho_{xx}} = A \exp\left(\frac{-2\pi^2\Gamma^2}{\hbar^2 w_c^2}\right), \text{ for Gaussian broadening,} \tag{1.18}$$

where A is a constant that depends on the relationship between conductivity and the DOS of the system. If $\log(\Delta\rho/\rho)$ varies linearly with $1/B^2$, then the LLs follow Gaussian broadening. If $\log(\Delta\rho/\rho)$ varies as $1/B$, then the broadening is Lorentzian. We can identify the closer fit between the two by making a so-called Dingle plot (Fig. 1.8). Here, A is extracted by taking the logarithm of either equation to find the linear fit. By log laws, A becomes the y-intercept in the linear equation $y = mx + b$ and so $A = 2$ if ρ_{xx} is proportional to the DOS, and $A = 4$ if ρ_{xx} is proportional to the square of the DOS.

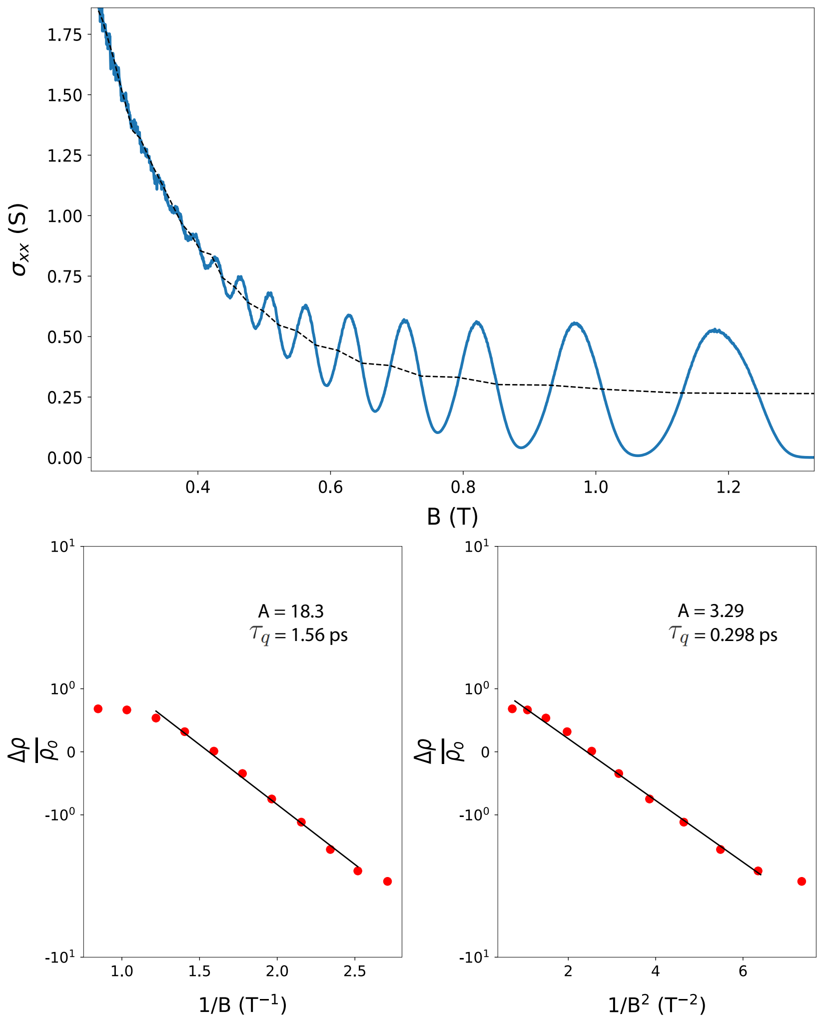

Figure 1.8 SdH oscillations and Dingle plots for sample VA141 in circular geometry (Corbino). Data from postdoctoral researcher Dr. Keyan Bennaceur in 2015. Top: The frequency of SdH oscillations in B is dictated by the quantum lifetime of the charge carriers in the 2DEG. By subtracting out the moving average (black), we can plot the amplitude. **Bottom:** Linear fits of the oscillation amplitude helps to ascertain whether the SdH follows Lorentzian (Middle) or Gaussian (Right) broadening. We find Gaussian broadening provides a closer linear fit and moreover, provides broadening values closer to previous findings [19], with $A = 3.29$, $\Gamma = 12.8$ K, and $\tau_q = 0.298$ ps.

1.3 Gated devices for Hall state interferometry

1.3.1 Interferometry

As we have reviewed in Section 1.1, measuring quantum Hall states requires manipulation of a magnetic field to alter the charge carrier density to magnetic flux ratio. An analogous and complementary technique is to apply voltages to deplete electrons locally [5]. Voltage can be applied using a range of types of gating configurations depending on the desired current path and device geometry. Interferometric gating allows more intricate current control to further investigate single particle interference or correlated particle many-body effects of the FQHE.

Interferometric systems for the QHE are comprised of a series of quantum point contacts (QPCs) arranged in order to transmit and reflect signals and measure interference. Common styles for the QHE are Mach-Zehnder [21, 22] or Fabry-Perot [23, 24], the latter used for the flip-chip devices here. A Fabry-Perot interferometer (FPI) is, in its most basic form, comprised of two sets of opposing QPCs with an additional plunger gate in between to control the area around which constricted current will flow [25].

1.3.2 Flip-chip device

Traditional interferometry fabrication methods involve depositing metal gating directly onto the wafer surface. The electron-beam (e-beam) deposition methods used involve heat and chemical processes to lay gates, which degrades electron mobility and introduces higher disorder into the wafer. To maintain pristine 2DEGs, we employ a special type of device known as a "flip-chip". This method involves a mechanical, rather than chemical, technique to connect the gates on a wafer. Another benefit of flip-chips is easy re-use and multi-use of

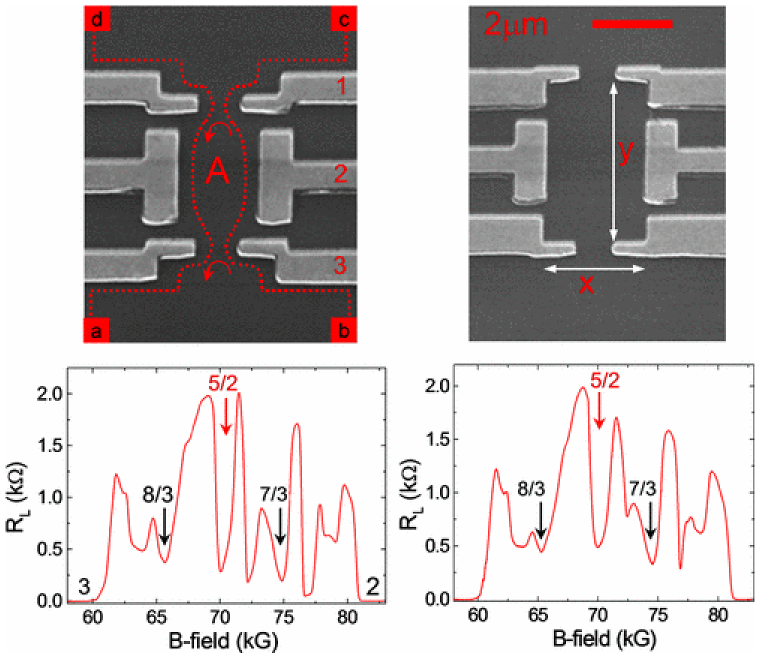

Figure 1.9 Two Fabry-Perot interferometers (FPI) on a GaAs/AlGaAs heterostructure. Top: two variations on two pairs of QPCs with two plungers in the middle provide the ability to vary applied voltages and confine current loops in the 2DEG, control electron interactions and fractional filling factors ν. Letters a-d indicate the contacts on the wafer's corners through which current is transmitted. **Bottom:** Longitudinal resistance as a function of B field shows fractional states for both interferometer designs. Figure from Willett *et al.* [20].

the same wafers, which are unique in quality and difficult to replace. This method is highly beneficial given the heterogeneity of mobility and charge carrier density across wafers.

Flip-chip gating is a known but uncommonly employed technique for studying the QHE [26] as well as other mesoscopic electronic systems [27]. The central tenet of flip-chip devices is the deposition of the metal gates or contacts on a separate substrate, which is then mechanically pressed on to the wafer under study to induce a field effect. In our flip-chip devices, thermally conductive and electronically insulative substrates are used to hold the gates, such as sapphire. A 10-30 nm coating of Al_2O_3 using atomic layer deposition (ALD) is added on top of the gates to prevent electric discharge from the gates to the wafer [28].

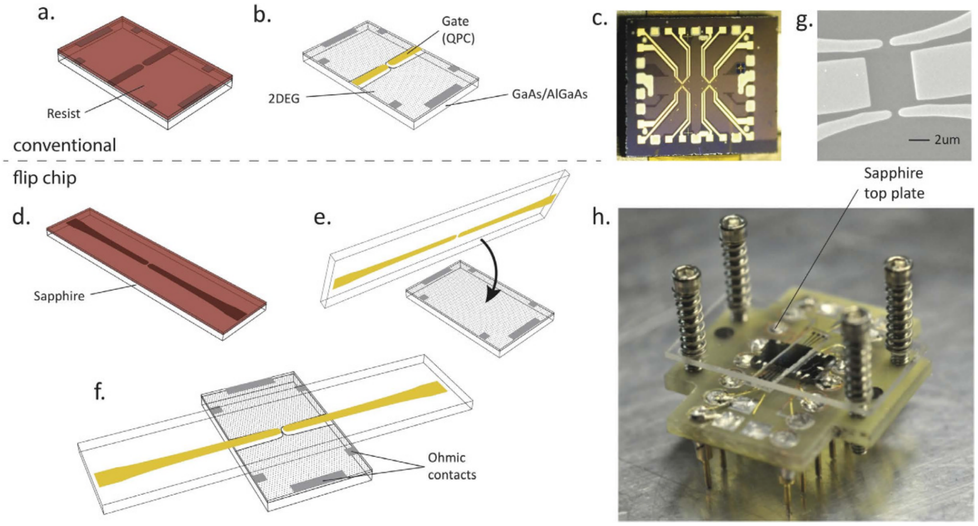

Figure 1.10 Conventional and flip-chip gating on semiconductor wafers from Bennaceur *et al.* [26]. **a., b., c.** With conventional gating, an e-beam and resist method is used to deposit metal directly on to the wafer. **d.,e.** Flip-chip gating uses a separate substrate upon which the metal gates are deposited. The substrate is then mechanically pressed on to the wafer. **f.** The only chemical process the wafer undergoes is to deposit or anneal ohmic contacts at the edges, leaving the central region where the gates act untouched. **g.** The gates are made with e-beam lithography resulting in highly precise, narrow gates in the tens of nano meters. **h.** The flip-chip device can be assembled with spring loaded screws and a large top sapphire plate to form contact between the wafer (black) and gates (transparent middle layer across the wafer).

Mechanically connecting the gates to the wafer prevents damage to the 2DEG from chemical deposition processes. Additionally, this modular design allows for easy disassembly leaving a pristine wafer for use in later experiments of different configurations.

The flip-chip gates can manipulate electron density in the wafer, and therefore sweep filling ratios by a field effect from the voltage applied to the metal tips (Fig. 1.10(f)). It is thought that the distance between gates and wafer cannot be greater than $\sim$100 nm before the electromagnetic field that reaches the 2DEG becomes to be too small to have any noticeable affect. To this end, there is significant technical difficulty creating functional flip-chip devices for studying the QHE, as discussed further below.

I assembled flip-chip devices to test and improve gating methods developed by past colleagues in the laboratory. The goal was to use the flip-chip techniques on higher mobility wafers that offer the potential to host fractional quantum Hall states but that are more difficult to induce a field effect in. Using flip-chip gating for the FQHE has not been previously published. I took old devices made on wafers from Dr. John Reno at Sandia National Laboratories (VA123) and Dr. Loren Pfeiffer at Princeton University (5.12.00.1). The flip-chip devices were made of four parts: the wafer in a rectangle for Hall bar geometry, a sapphire piece with the metal gates made of titanium and gold with nickel (∼150 nm thick) and coated with insulating PMMA (∼20 nm) to prevent electric discharge from the gates, another piece of sapphire on top to press the gates down, a G10 plastic board with pins to plug on to the refrigerator headers, and spring-loaded screws holding the assembly (Fig. 1.10 h.).

The previously constructed devices had accumulated a lot of dirt over their three to five year lifespan, adding the risk of misalignment of the gates with the wafer (see dirt in Fig. 1.11). I cleaned and reassembled the devices, then attempted to pinch off longitudinal conductance σ_H. I used an Oxford He3 refrigerator to cool the devices without a magnetic field to see if the gates were functioning before using a refrigerator with a magnetic field to measure Hall states. My devices were made with Hall bars, which are long rectangles comprised of a series of equal squares. With this configuration, longitudinal resistance or conductance can be converted to resistivity or conductivity by dividing by the area in between the ohmic contacts.

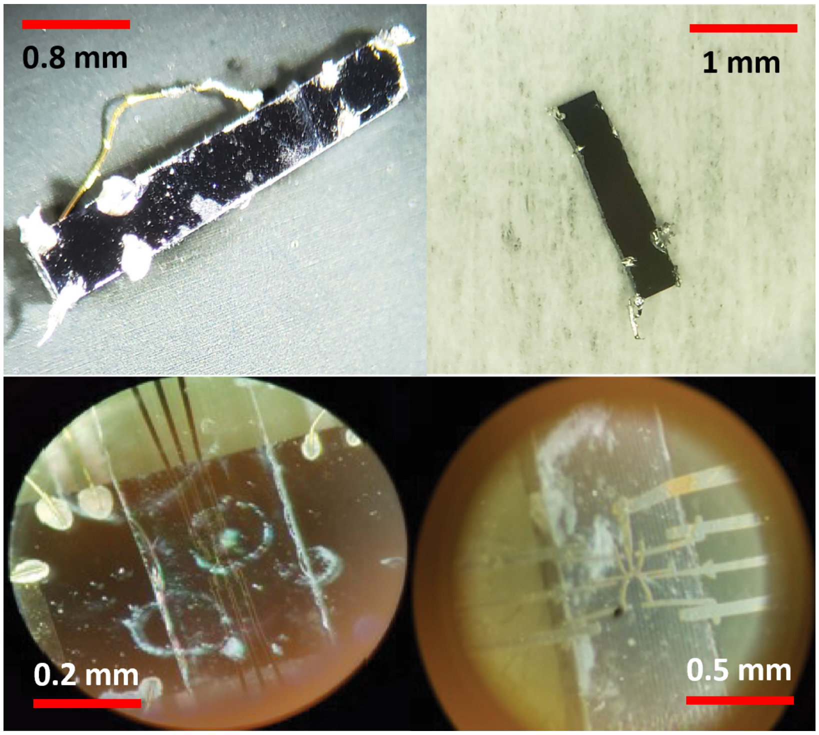

Figure 1.11 Dirt accumulated on various parts of the wafer (PF 5.12.00.1) and gates. Top left: The Hall bar wafer had significant dust and grease accumulated since original construction. **Top right:** Once cleaned (see Appendix B), some ohmic contacts fell off requiring re-annealing. **Bottom left:** Residue, perhaps evaporated liquid, rests on the sapphire substrate that hosts the gates. **Right:** Grease on the wafer, before disassembly, could create too large a gap between gates and heterostructure.

To pinch off the gates, I applied voltages from -40 V to +40V on opposing FPI gates to create an electric field effect depleting electrons in the area between the ohmic contacts. I was unable to notice a significant change in conductance and have no indication of whether there was any field effect present. I then mounted different gates with two QPCs without plungers and scanned from 0 to -120V and 0 to +120 V again with no clear sign of electron depletion (Fig. 1.12).

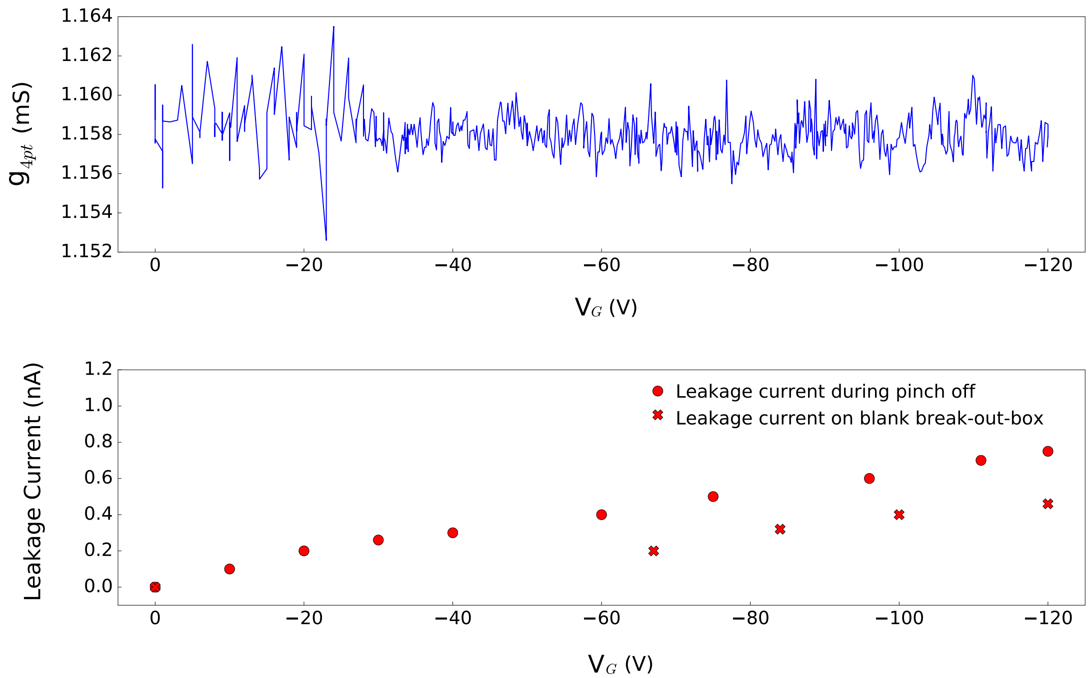

Figure 1.12 Attempted conductance pinch off of flip-chip d evice (PF 5.12.00.1). Top: Conductance as a function of gate voltage (noise floor ∼0.003 mS, median conductance ∼1.158 mS). Voltage increase should displace electrons reducing conductance, however no decrease is seen. **Bottom:** Leakage current measured simultaneously with conductance (circle) compared with leakage current measured with voltage applied only to the breakout box (cross).

1.3.3 Postmortem analysis

Even though I thoroughly cleaned the wafers and worked on mechanically aligning the gates on the sapphire flat on the wafer, I was unable to observe electron depletion marked by a reduction in conductance. There are a number of possible reasons for this, as discussed below.

It is unlikely that the gates were leaking since I measured leakage at the breakout box with an applied voltage both while measuring the 2DEG's conductance and later on the breakout box without the flip-chip and with non-grounded plugs (Fig. 1.12 Bottom). Even with the 2DEG connected, the gates are designed to function as charged metal rods, that is, they create a field effect and there should be no current running from gates into the wafer, to ground, or to the breakout box. Leakage current during attempted pinch off is within $\sim 5\%$ of the leakage current with the breakout box on its own, suggesting that there were no current leaks between the gates and the breakout box, wafer, or ground.

It is possible that the gates were not parallel or close enough to the wafer surface and 2DEG beneath. Dirt in between the gates on the sapphire substrate and the wafer is a common cause for misalignment. Particles of dust $\sim$5 microns in diameter are ubiquitous in the laboratory environment and could separate the gates from the wafer preventing a field effect from reaching the 2DEG. Even with cleaning for dust and grease, another cause for misalignment could be an uneven surface on the wafer or bumps on the fabricated gates on the sapphire. One way to confirm proper alignment in a flip-chip device is by looking at Newton rings. These rainbow wave patterns are visible to the naked eye and can form from light reflected between the GaAs wafer and the sapphire. If there is no angle in the space in between the substrates, there would only be one colour of light visible on the substrate. More stripes of different colours would indicate misalignment, such as circular Newton rings surrounding a large dust particle. It is possible to use these Newton rings to identify lack of parallelism and to adjust the four-point spring-loaded screws. I did not find any such circles, although I did see wide banded Newton rings after considerable number of attempts to remove them.

It is possible that the gates received an electric shock from static discharge, which has happened with other sets of gates (Fig. 1.14). It is hard to know exactly when in the fabrication and assembly process large enough electric discharge could burn the gates. It is possible to occur from human touch if the person is not grounded and if they have accumulated static charge. For example, walking can contribute to static discharge on the order of thousands of

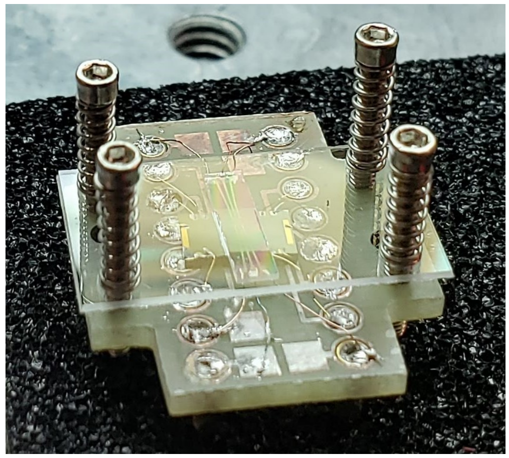

Figure 1.13 Newton rings visible on the flip-chip device to the naked eye. A single curved rainbow is visible across the device with one tone over the area of the FPI gates. Wide, non-repeating colour bands such as these indicate better alignment.

Volts [29]. However, the extreme caution used when handling the devices leaves little possibility for direct handling errors. Care was taken to ensure connections between the device fixed on the refrigerator and the breakout box were both grounded in between measurements and that I was connected to the lab's grounding source when taking data. There is a chance the gates were burnt through electrostatic shock while cleaning the sapphire, although they were inspected under microscope before being mounted on the wafer afterwards (an example of burnt gates is shown in Fig. 1.14).

A final consideration is whether the noise level in the experiment was too high to measure pinch-off of conductance. This scenario is unlikely, if the device, cryostat, and voltage and current meters can be compared to that of previous work [26]. Bennaceur and co-workers measured a decrease from $\sim$3 to $\sim$0 e^2/h. I measured a baseline of $\sim$1.158 mS ($\sim$0.03 e^2/h) on a four-point measurement. Since my noise floor $\Delta S \simeq 0.005$ mS, I should have been able to see conductance decrease if a significant field effect was present.

Future flip-chip measurements would be well served by fabricating brand new gates on

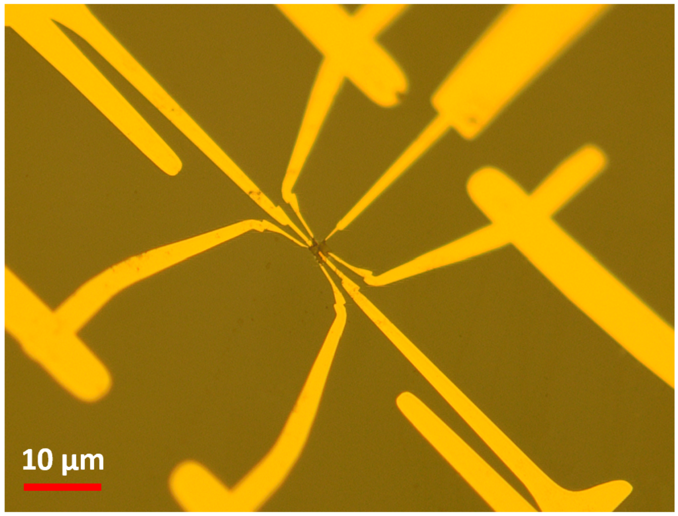

Figure 1.14 Microscope image of burnt FPI gates with an additional plunger on the side. At the convergence of the gates in the center, where the gates act on the 2DEG, lies a dark brown spot with now truncated metal tips. This is indicative of an electric shock that burnt off the tips of the thin metal gates.

sapphire, which was scheduled for Winter 2020 until the laboratory closure due to COVID-19. It could be that the 10's of nanometers of Al_2O_3 ALD became rough or otherwise damaged over the years since fabrication and was unable to be properly cleaned. A fresher coat might help achieve a closer and flatter fit between wafer and gates.

Chapter Two

Quantum Faraday Effect

The Faraday effect is the optical analogue of the Hall effect. The Hall effect is the generation of an electric field $\mathbf{E}_H$ transverse to the direction of current flow I and magnetic field B caused by the Lorentz force (Fig. 2.1 (Left)). The Faraday effect also arises from the action of Lorentz force upon a charge, ultimately resulting in the rotation of polarization plane of a linearly polarized electromagnetic wave (Fig. 2.1 (Right)). We define θ_F as the angle of linear polarization rotation with respect to the incoming wave polarization. In many materials, Faraday rotation is weak and well described by a linear relation $\theta_F = VdB$, where V is the Verdet constant and d is the thickness of the medium.

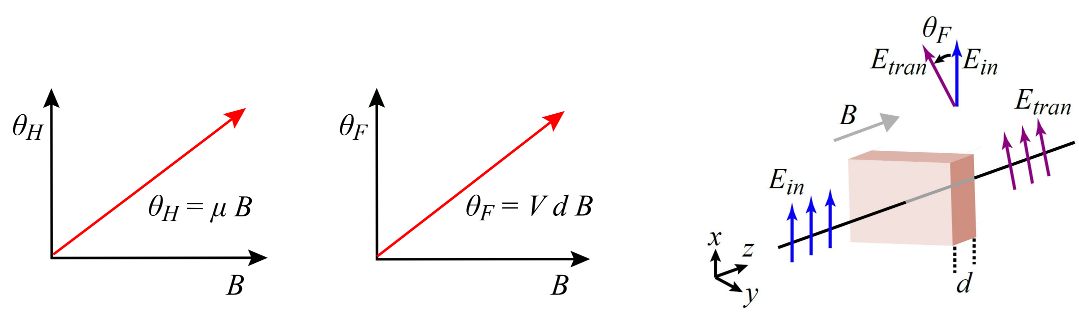

Figure 2.1 Hall and Faraday rotation. Left: Classical Hall and **Middle:** classical Faraday rotation as a function of magnetic field B. **Right:** Cartoon of Faraday rotation through a material [4].

As we will show in this work, the high-mobility 2DEG enables a giant single pass rotation of $\theta_F \simeq 45^\circ$ ($\simeq 0.8$ rad) at the crossover between the low and high magnetic field regimes and robust plateaus observed at quantized filling factors with Hall indexing i$= 2, 3, 4...$ in high magnetic fields (1 T $< B <$ 6 T). This chapter provides an overview of past research and a derivation of quantized angles of Faraday rotation as well as a recent study.

2.1 Derivation of Faraday angle of rotation in a 2DEG

Rotation of the Faraday angle of linearly polarized microwaves can be arrived at from simple theories for microwave transmission in space. We can begin with the transmission of an electric mode through a medium, here a semiconducting sheet with a 2DEG, in free space. Charge carriers are subject to a Lorentz force in the presence of applied electromagnetic fields,

$$F = -e(\mathbf{E} + \mathbf{v} \times \mathbf{B}), \tag{2.1}$$

where $\mathbf{E}$ is a electric field in the xy plane with charge carries of velocity $\mathbf{v}$ and $\mathbf{B} = B_0\hat{z}$ is the applied magnetic field applied perpendicular to the sheet. The electric field from the signal at frequency ω induces an alternating current $j_x = \sigma_{yx}E_y$ in the 2D layer [30]. This current induces another electromagnetic field and so on. The induced currents and electromagnetic fields accumulate a phase and the angle of rotation θ_F of this polarization of the outgoing wave is given by,

$$\theta_F = \tan^{-1}(\frac{E_y}{E_x}). \tag{2.2}$$

The electromagnetic wave can be described as possessing left and right -handed transmission $t_\pm = t_x \pm it_y$ that depends on the sheet conductivity. From Fresnel coefficients [31], the transmission through a medium with a refractive index n is,

$$t_{\pm} = \frac{2}{1+n+Z\sigma_{\pm}}, \tag{2.3}$$

where $Z = Z_0 = 377\ \Omega$ is the mode impedance in free space, and $\sigma_{\pm} = \sigma_{xx} \pm i\gamma\sigma_{yx}$ is the sheet conductivity (in free space, $\gamma = 1$). We can express the Faraday angle as

$$\tan(\theta_F) = \frac{t_y}{t_x} = \frac{1}{i}\left(\frac{t_+ - t_-}{t_+ + t_-}\right) = \frac{1}{i}\left(\frac{\frac{1}{t_-} - \frac{1}{t_+}}{\frac{1}{t_-} + \frac{1}{t_+}}\right). \tag{2.4}$$

Plugging in (2.3),

$$\tan(\theta_F) = \frac{1}{i}\frac{1+n+Z\sigma_- - (1+n+Z\sigma_+)}{1+n+Z\sigma_- + (1+n+Z\sigma_+)} \tag{2.5}$$

$$= \left(\frac{1}{i}\right)\frac{Z(\sigma_- - \sigma_+)}{2(1+n) + Z(\sigma_- + \sigma_+)} \tag{2.6}$$

$$= \frac{Z\sigma_{yx}}{1+n+Z\sigma_{xx}}, \tag{2.7}$$

which is equal to $\tan(\theta_F) = \frac{Z\sigma_{yx}}{2+Z\sigma_{xx}}$ in free space ($n = 1$), and $-\sigma_{xy} = \sigma_{yx}$. If in the quantum Hall regime, conductance becomes $\sigma_{xx} = 0$ and $\sigma_{yx} = \mathrm{i}e^2/h$, where i$= 2, 3, 4, 5...$ is the integer quantum Hall filling factor. The conductance matrix takes the form

$$\vec{J}(\omega) = \hat{\sigma}\vec{E}(\omega) = \begin{pmatrix} 0 & -\mathrm{i}e^2/h \\ +\mathrm{i}e^2/h & 0 \end{pmatrix} \vec{E}(\omega). \tag{2.8}$$

Then, as first found by Volkov and Mikhailov in their 1985 seminal work [30], the expression for quantized Faraday angle through a material in free space ($Z = Z_0$) becomes

$$\tan(\theta_F) = \frac{Z_0(\mathrm{i}e^2/h)}{2 + Z_0(0)} = \frac{\mathrm{i}Z_0e^2}{2h} = \mathrm{i}\alpha, \tag{2.9}$$

where $\alpha = Z_0 e^2/2h \simeq 1/137$ is the fine structure constant. This prediction is seen in subsequent sections to elegantly describe the data from our current work, even when electromagnetic confinement is introduced.

2.2 Previous experimental works

First discovered classically in 1846 [32], Faraday rotation manifests itself in a wide range of physical settings, from engineering on Earth to light from stars in outer space [33, 34]. Faraday rotation can be seen weakly in many materials in two- and three-dimensions. Research on the Faraday effect within condensed matter physics and engineering offer new insights into non-reciprocal electromagnetic responses of materials. One application of this is for circulators and isolators, which traditionally rely on ferrimagnetic ceramics which exhibit static behaviour not tunable by external voltages [35]. Another source of motivation for low-dimensional Faraday experiments is for optical manipulation of electron motion.

Recently, both experimental [36] and theoretical research has offered promising suggestions for utilizing Faraday rotation for quantum phase gates [37]. Additionally, further research goals have been established for utilizing quantized Faraday rotation for quantum computation applications [36, 38].

2.2.1 Microwave experiments (GHz)

In the late 20^{th} century, researchers studied electromagnetic wave frequencies ω in the regime $\omega < \omega_c$, where $\hbar\omega_c$ is the characteristic amplitude of the impurity potential with ω_c the frequency of the cyclotron motion of the charge carriers in the material. Volkov *et al.* published a theoretical work outlining Faraday rotation in free space, where $\theta = e^2/\hbar c = 1/137$ deg [30]. Volkov and collaborators then documented the first evidence for the quantization of the Faraday effect in a two-dimensional electron system in GaAs in an uncalibrated setup [39]. This work was conducted at low-frequencies when Landau levels are present in the 2DEG system when subjected to a large magnetic field. Volkov and Mikhailov suggest that the Faraday effect is dictated by conductivity. They propose that quantum Faraday rotation could elucidate the dispersion of $\sigma_{yx}(\omega)$, the Hall conductance as a function of the frequency of microwave or other light [30].

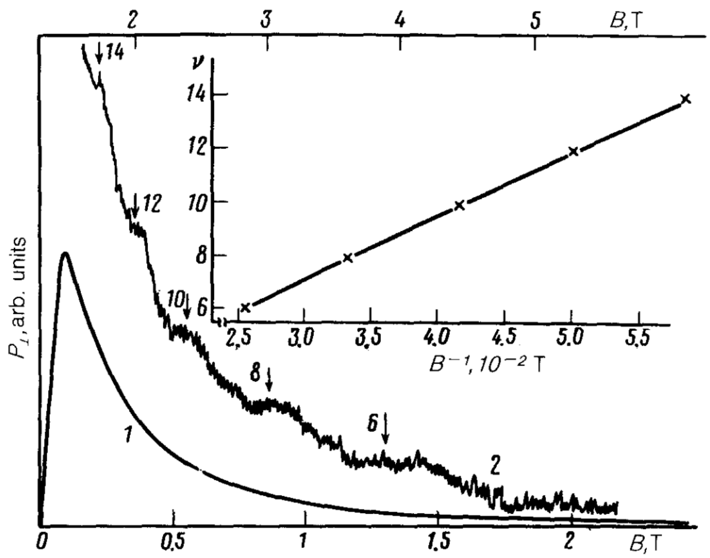

Figure 2.2 Findings from Volkov *et al.* of uncalibrated, quantized Faraday rotation [39]. Polarization plane (P) versus magnetic field B at low (high) field on the lower (upper) curve. Hints of plateaus in the polarization are shown with arrows. **Inset:** Density $n = 5.8 \times 10^{11}$ cm^{-2} was extracted from the Landau fan.

A small number of experiments with microwaves have since been conducted, including Skulason and colleagues' study using field effect tuning in Faraday rotation of microwaves (~20 GHz) in graphene [35]. Sounas and colleagues show transmission and reflection amplitude as a function of frequency and conductivity as a function of magnetic field from 0 to 5 T suggesting that single layer graphene could be a good candidate for hosting giant Faraday rotation of microwave signals [40].

2.2.2 Optical Experiments (THz)

Recent quantized Faraday rotation measurements have been conducted in the optical terahertz (THz) range, where $\omega \simeq \omega_c$. All experiments to date have been at low temperatures, *i.e.* close to, or below the liquefaction point of Helium (∼4.22 K).

Mittleman and colleagues used THz signals as a non-contact method for measuring Hall states in GaAs [41]. Exploiting the small difference between ω_c and the THz signal frequency, researchers mapped out charge carrier density and mobility spatially on the sample without the need for attaching any potentially damaging contacts. Ikebe and colleagues used THz signals to probe $\sigma_{yx}(\omega)$ resulting in plateaus in conductance around ν = 2,4,6 in a modulation-doped GaAs/AlGaAs heterostructure [42].

Crassee and colleagues use single atomic layer graphene to provide rotation of polarization of THz light of $\sim 6^o$ [38]. Shimano and colleagues conducted a similar study on monolayer graphene with electron density $n = 2.2 \times 10^{11}$ cm^{-2} [43]. They observe hints of integer filling from rotated Faraday angle and a magneto-optical Kerr effect between graphene and a silicon substrate. Wu and colleagues show Faraday rotation in Bi_2Se_3 following the fine structure constant within 0.4% of its known value [44]. This bismuth selenide material was used for its topologically insulating properties with THz pulses resonating through the thin film resulting in both Faraday and Kerr rotations.

Shuvaev and colleagues use HgTe quantum wells grown on GaAs to observe quantized Faraday angle rotation using Mach-Zehnder interferometry [45]. Plateaus in Faraday rotation is observed in steps of $\sigma_{yx} = e^2/h$. Dziom and colleagues use 2D topological surfaces at the boundaries of a 3D HgTe on CdTe sample with density $\sim 10^{11}$ cm^{-2} to measure Faraday and Kerr rotation [46]. Their study hints at quantized σ_{yx} and attributes Faraday rotation equal to the fine structure constant to topological magnetoelectric effects of the material.

2.3 McGill-Sherbrooke collaborative work

A study was conducted collaboratively between laboratories located at McGill and Sherbrooke to further investigate Faraday rotation in the microwave regime [4]. A giant single pass rotation of $\theta_F \simeq 45°$ ($\simeq 0.8$) rad at the height of the classical regime was measured as well as quantized Faraday rotation with Hall indexing i$= 2, 3, 4...$ in high magnetic fields (1 T $< B <$ 6 T).

2.3.1 Experimental setup

The Faraday rotation was measured inside a hollow circular waveguide with a diameter of 23.825 mm. The waveguide is made out of silver plated brass and the orthomode transducer is silver plated copper.

Figure 2.3 Metal waveguide utilized for the Sherbrooke Experiment (photo by V. Suresh). An electric diode in the left most piece emits the microwaves, which passes through the wafer held in the waveguide in between the middle sections, is split into orthogonal modes by the orthomode transducer, and is sent back to the vector network analyzer (VNA).

A ∼10 mm × 10 mm piece of a GaAs/AlGaAs wafer (VA141) grown by Molecular Beam Epitaxy (MBE) at Sandia National Laboratories by Dr. John Reno was placed inside the waveguide. The wafer was fixed with vacuum grease on to a custom-designed copper piece, which screwed in between circular waveguide sections. The copper insert is fitted with a 9 mm diameter circular iris for the microwaves to pass through the wafer. The iris' small diameter compared with the waveguide diameter of 23.825 mm is due to the constraint of a 10 mm square wafer size.

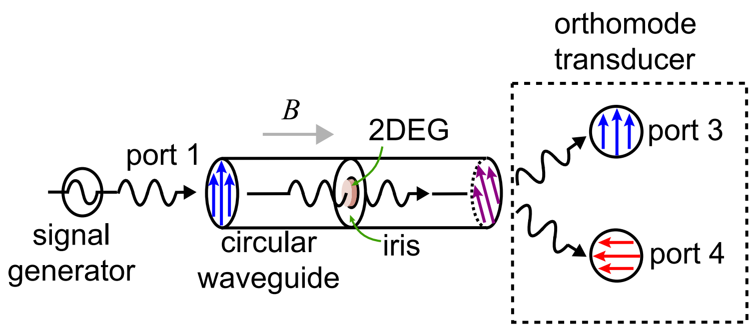

Figure 2.4 Experimental setup of Faraday microwave rotation. A linearly polarized electromagnetic wave is injected into a circular hollow waveguide (port 1) that supports two orthogonally polarized TE_{11} modes. The transmitted field is measured using an orthomode transducer in a direction parallel (port 3) and perpendicular (port 4) to the incoming electromagnetic wave [4].

The assembly was housed in a BlueFors dry dilution refrigerator with the waveguide inserted vertically in the 4" bore of a superconducting solenoid magnet with positive (+) direction aligned with the direction of propagation of the incident microwaves. This refrigerator has a base temperature of ∼7 mK at the cold plate, to which the waveguide assembly was thermally anchored. While there was no direct measurement of the temperature of the 2DEG, the following comparison of Faraday rotation at different mixing chamber temperatures (Fig. 2.6) suggests the electron bath to be cooled to at least ∼200 mK.

Faraday rotation was induced by applying a ± 6 T magnetic field in the direction of the waveguide length with the superconducting solenoid surrounding the refrigerator's tail. For the microwave experiment, a linearly-polarized electromagnetic wave was injected via port 1 into the waveguide. Supporting two orthogonally polarized TE_{11} modes, the output signal is split orthogonally via an orthomode transducer which transmits the output power to a vector network analyzer (VNA) (Fig. 2.4).

2.3.2 Experimental data

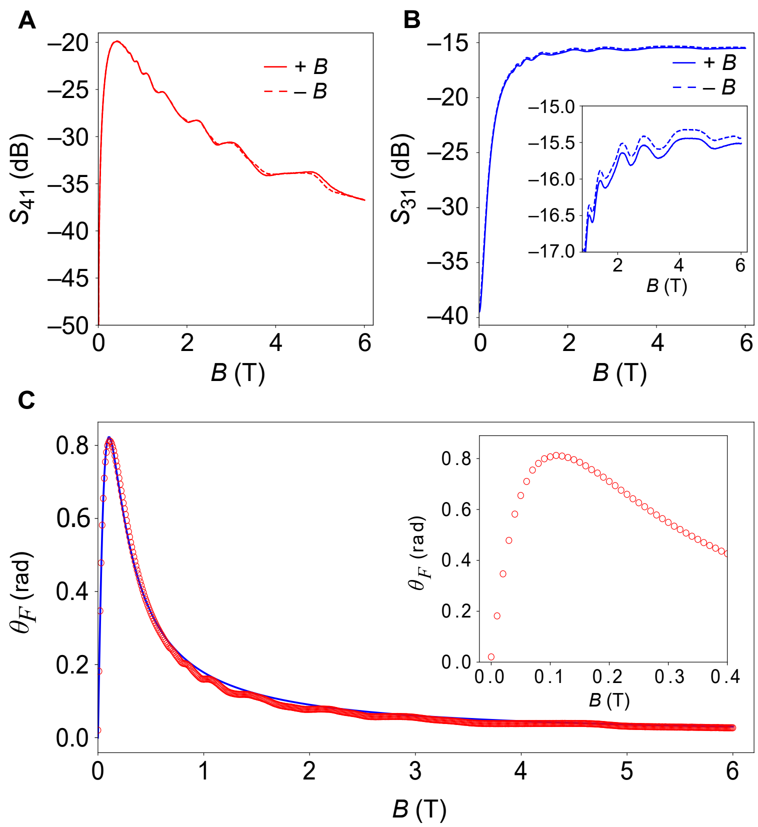

Figure 2.5 Faraday rotation through the 2DEG. A) Perpendicular port scattering parameter S_{41} and **B)** Parallel port scattering parameter S_{31}. The solid (dashed) line denotes the positive (negative) magnetic field polarity along the waveguide length. **C)** Magnetic field dependence of Faraday angle θ_F at base temperature of the dilution refrigerator ($\sim$7 mK). The blue line demonstrates a close fit to a classical Drude conductivity model. The inset portrays a zoom in of the same data at the largest point of Faraday rotation, between low and high field regimes.

Data was collected at Université de Sherbrooke using two out of four-ports of an Agilent PNA-X VNA. The Faraday angle was determined by measuring the amplitude of transmission scattering parameters (s-parameters) of the two orthogonal the TE_{11} modes. $|S_{41}|$ is the amplitude of the transmitted signal perpendicular to the waveguide length and $|S_{31}|$ is parallel. Data collected in decibels (dB) was converted to linear scale to obtain the modulus of the tangent of the signal, $|\tan(\theta_F)| = \frac{S_{41}}{S_{31}}$. The VNA also measures phase ϕ, which can be used to construct the complex signal from $tan(\theta_F) = |\tan(\theta_F)|e^{i\phi}$. Magnetic field strength was recorded simultaneously directly from the magnet source.

2.3.3 Electromagnetic confinement

A quantitative model for the observed Faraday rotation can be obtained by combining a simple theory for microwave transmission in a system with electromagnetic confinement, along with a Drude conductivity model for the 2DEG. From a linear *ansatz* from the transmitted electric fields, it can be shown [4] that Faraday rotation in a waveguide loaded with a 2DEG is generally given by

$$\tan(\theta_F) = \frac{\gamma Z \sigma_{yx}}{K + Z\sigma_{xx}}, \tag{2.10}$$

where Z is an effective wave impedance, K is an effective transmission coefficient, and γ is a mode coupling parameter. For simplicity, we assume that $Z, K \in \mathbb{R}$. A similar relation was developed and applied to experiments for a simple hollow waveguide geometry without an iris [35, 40]. In the idealized free-space scenario, $Z = Z_0 = 377\ \Omega$, $K = 2$, and $\gamma = 1$, however these values will be modified in the presence of electromagnetic confinement. Notably, Eq. (2.10) is general, applying even in the presence of an iris where the near-field distribution defies a simple analytical solution [47].

2.3.4 Classical Drude model

We now wish to develop an understanding of Faraday rotation θ_F in the electromagnetic confinement of our waveguide as a function of conductivity σ. To achieve this, we utilize a simple classical Drude conductivity tensor for our 2DEG system,

$$\hat{\sigma}^D = \sigma_0 \frac{1}{(1-i\omega\tau)^2 + (\omega_c\tau)^2} \begin{pmatrix} 1-i\omega\tau & -\omega_c\tau \\ \omega_c\tau & 1-\omega\tau \end{pmatrix}, \tag{2.11}$$

where $\sigma_0 = ne^2\tau/m^* = ne\mu$ is the Drude conductivity and ω_c is the cyclotron frequency related to the charge carrier scattering time τ and $\omega_c\tau = \mu B$. In our experiment, $\tau = m^*\mu/e \simeq 38$ ps from the mobility of our wafer, $\mu \simeq 1 \times 10^6$ cm^{2}V^{-1}s^{-1}, which was measured using the methods presented in Chapter 1 Section 2. As can be seen in Fig. 2.5C, by the blue line, this simple model here accurately captures the essential features of Faraday rotation θ_F over the full range of magnetic field B.

Inserting the Drude model for conductivity inside Eq. (2.7) for $\tan(\theta_F)$ gives

$$\tan(\theta_F) = \frac{\gamma Z \sigma_o \omega_c \tau}{|K[(1-i\omega\tau)^2 + (\omega_c\tau)^2] + Z\sigma_o(1-i\omega\tau)|}. \tag{2.12}$$

In the low magnetic field regime, where $\omega_c\tau = \mu B \ll 1$, $B \to 0$, $\omega_c\tau \to 0$, $\sigma_{xx} \to \sigma_o$, $Z\sigma_o \gg K|1-i\omega\tau|$. Therefore, $\tan(\theta_F) \simeq \frac{\gamma\omega_c\tau}{|1-i\omega\tau|} = \frac{\gamma\mu B}{|1-i\omega\tau|}$, where in our experiment, $|1-i\omega\tau| = 2.79$. As a result $\theta_F \propto B$ for $B \ll 100$ mT, as is observed experimentally and shown in Fig. 2.5. In the high magnetic field regime, where $\omega_c\tau = \mu B \gg 1$, $\tan(\theta_F) \simeq \frac{\gamma Z \sigma_o}{K\omega_c\tau} = \frac{\gamma Z}{K}\frac{ne}{B}$. Here, the rotation $\theta_F \propto 1/B$, as is coarsely observed for $B \gg 100$ mT. To more closely describe Faraday rotation in the high field regime, analysis that considers quantization of the transverse (Hall) conductivity is required.

2.3.5 Integer quantum Faraday effect

We can arrive at an expression for quantized Faraday rotation in the high field regime by applying, as discussed earlier, our simple model from Eq. (2.9) in the quantum regime when

Landau levels are present. Volkov and Mikhailov's 1985 calculation for quantized Faraday rotation in free space [30] yields,

$$\tan(\theta_F) = \frac{\mathrm{i}e^2}{c\hbar} = \mathrm{i}\alpha, \tag{2.13}$$

where c is the speed of light in vacuum. This is the consequence of the vanishing longitudinal $\sigma_{xx} = 0$ and quantized transverse conductance σ_{yx}, where in the IQHE, σ_{yx} becomes quantized following the integer filling number i$= 2, 3, 4, 5, 6$ which goes as $1/B$. In an electromagnetic confinement in the quantum regime $\sigma_{xx} = 0$ and $\sigma_{yx} = \mathrm{i}e^2/h$.

When $\omega \ll \omega_c$, as is the case with $\omega = 1.12 \times 10^{10}$ Hz microwaves compared with $\omega_c = \mu B/\tau \simeq 10^{17}$ Hz, Faraday rotation quantization takes a modified form by substituting into Eq. (2.10) σ_{xx} and σ_{yx} in the quantum Hall regime:

$$\tan(\theta_F) = i\frac{\gamma Z}{K}\frac{e^2}{h} = i\alpha*, \tag{2.14}$$

where $\alpha*$ is a "fine structure constant" in a non-idealized, non-free space scenario and γ, Z, K are electromagnetic confinement parameters specific to the experimental geometry and frequency. Here, $\gamma \in [0, 1]$ is a mode coupling factor found by taking the slope of the Faraday rotation at low magnetic field. Eq. (2.14) is approximately correct without inclusion of the refractive index of the bulk medium in a sample with thickness d small compared with wavelength λ. In our case $d \simeq 0.5$ mm and $\lambda \simeq 2.7$ cm providing a ∼50 times difference.

The measured Faraday rotation angle tangent $\tan(\theta_F)$ is plotted versus $1/B$ (solid red line) in Fig. 2.6. Six plateaus are clearly observed in $\tan(\theta_F)$ versus $1/B$, with the lowest three plateaus evenly spaced along both axes, and a further three evenly space plateaus are observed with twice the step height. We confirm the origin of these Faraday rotation plateaus with the emergence of Landau levels (LLs) by plotting a fan diagram of the assigned LL index i for each plateau versus the reciprocal field $1/B$ of the mid-point of each plateau. The

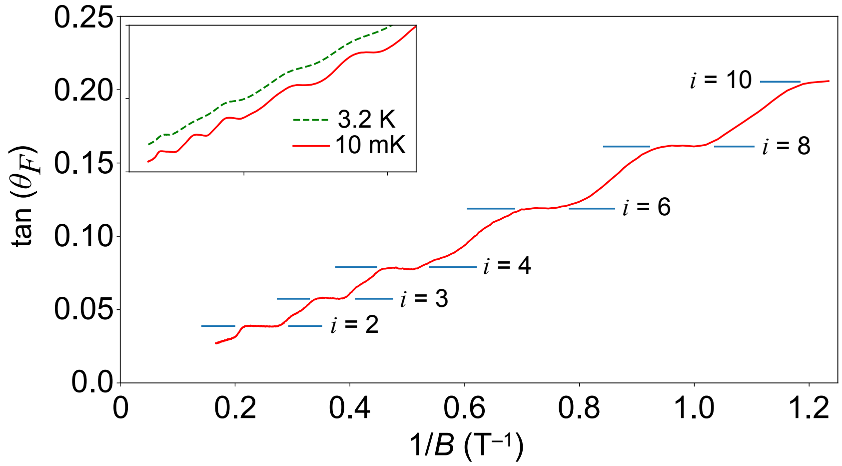

Figure 2.6 Faraday angle in the high magnetic field regime. Here $\tan(\theta_F)$ is plotted versus $1/B$ (solid red line) at the base temperature of the dilution refrigerator. The expected position of each observed Faraday plateau is shown by horizontal markers with the quantization condition $\tan(\theta_F) = \mathrm{i}\alpha^*$. **Inset**: temperature dependence of the plateaus and smudging of quantization at higher temperatures.

observed integer filling factor sequence i$= 2, 3, 4, 6, 8...$ follows the LL filling factor relation i$= \frac{nh}{eB}$ with an electron density 2.08(5) x 10^{11} cm^{-2}, consistent with quasi-DC transport studies performed on samples of the same semiconductor wafer hosting the 2DEG. Here, the expected spin degeneracy lifting of the LLs occurs in between integer filling i$=$ 4 and 6, at a magnetic field value B $\sim$1.8 T again consistent with previous quasi-DC charge transport studies of 2DEGs hosted in similar heterostructures with comparable electron mobility and density. A linear fit of the indices provides a close to zero intercept of -0.06(6). This is in keeping with other studies of quantized Hall states in GaAs, a material that normally lacks a y-axis intercept or Berry phase [48, 49].

The Faraday rotation was also measured during a separate cool down in a slightly different experimental configuration employing two coaxial assemblies. These measurements are shown in Fig. 2.6 (inset) with the temperature of the dilution refrigerator at 10 mK (red

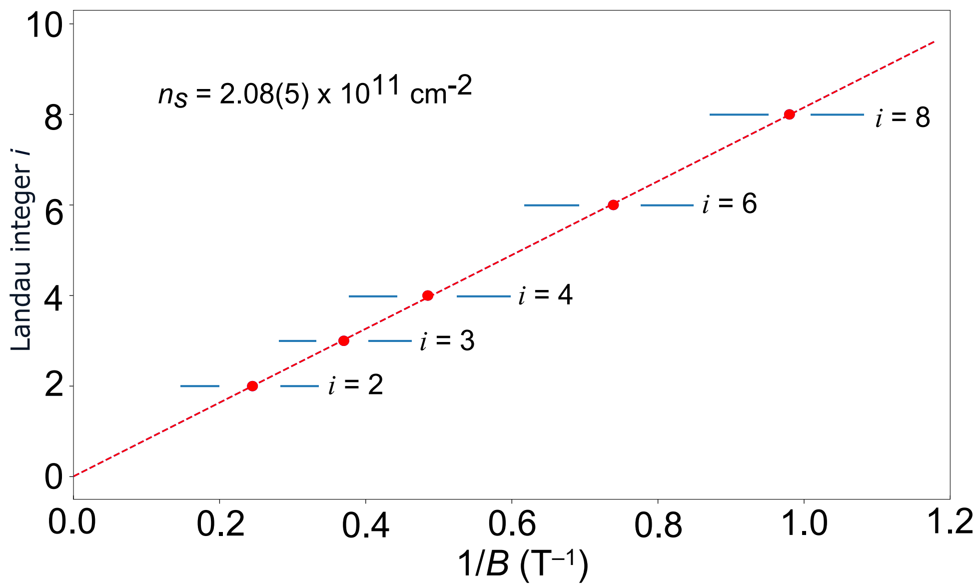

Figure 2.7 Landau level index i versus plateau mid-points in $1/B$ (red circles). The 2DEG electron sheet density n_s is inferred from the linear fit of the points (dashed line). An insignificant intercept of -0.06(6) is present.

line) where quantization is visible, and at 3.2 K (blue line) where quantization is almost absent. In the quantum Hall regime, at temperatures $k_B T$ approaching the LL energy gap Δ, thermal excitation of electrons across Δ gradually overpowers conductivity quantization until it is ultimately absent. In our measurements, the plateaus of Faraday rotation θ_F cannot be resolved at 3.2 K, consistent with orbital quantization present in the 2DEG caused by a strong magnetic field.

2.3.6 Extraction of α*

We have established that the rotation of polarization of microwave signal θ_F is related to the fine structure constant α. We have seen that the quantization in free space $\tan(\theta_F) = \mathrm{i}\alpha$ will differ from that in the presence of electromagnetic confinement, $\tan(\theta_F) = \mathrm{i}\alpha^*$. From a linear fit of the mid-points of each plateau in $\tan(\theta_F)$ versus $1/B$ (Fig. 2.7), the experimentally observed rotation quantum is $\alpha^* = 0.0204(3) = 2.80(4)\alpha$. This is not surprising as the quantum of rotation in an ideal free-space scenario is α, and electromagnetic confinement is expected to modify wave impedance and field distribution such that the rotation quantum in general should differ from its free-space value, $\alpha^* \neq \alpha$.

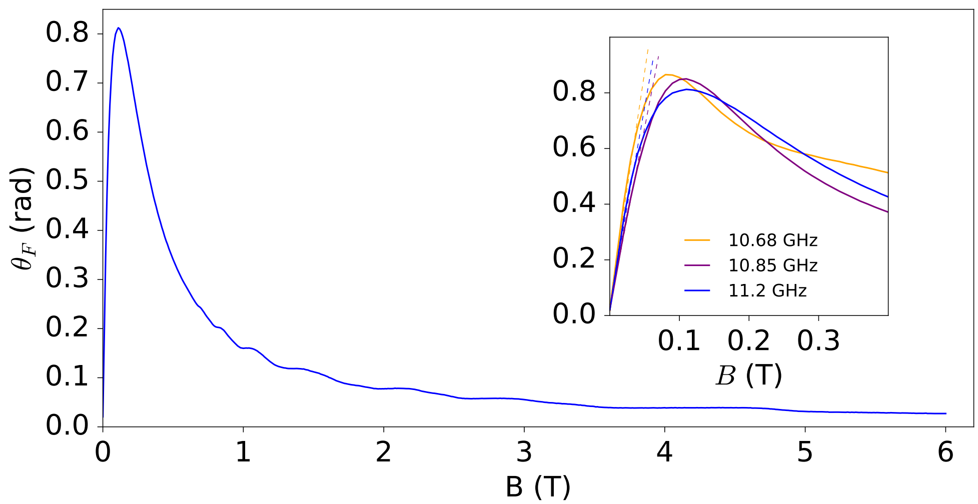

Figure 2.8 Extraction of γ from the linear classical Faraday regime at low magnetic fields. $\tan(\theta_F)$ is shown plotted versus B from which the prefactor γ can be extracted from the linear low field regime (inset). The inset provides a closer look at the classical regime and shows slope has a very slight but somewhat unclear frequency dependence requiring further investigation.

We can compare calculated and measured values of α^* by looking at Eq. (2.14) and extracting α^* from our data. Since gamma is a prefactor of Eq. (2.14), the slope of the linear regime which resides at low field is $\gamma Ze^2/Kh$ (Fig. 2.8). Once γ is extracted from the low field regime, we can input its value to solve for Z/K as a fit parameter for the entire curve. In our experiment, the best fit fixes $Z/K = 1192(3)\ \Omega$ and $\gamma = 0.49(1)$. Solving for α^* in Eq. (2.14) we obtain $\alpha^* = 3.10(2)\alpha$, agreeing within 10% of our measured and extracted value of $\alpha^* = 2.80(4)\alpha$.

We have observed robust measurements of quantized Faraday rotation with well-formed plateaus at integer filling. We have measured the quantization of Faraday rotation in the quantum Hall regime in a high-mobility 2DEG. Microwave Faraday rotation plateaus are robust and well formed, allowing Landau level indexing and the observation of a spin-splitting structure. Measurement of microwave Faraday rotation is thus a contactless method that may prove useful in probing low-dimensional electronic phenomena such as the quantum spin Hall effect [50], the quantum anomalous Hall effect [51], and the fractional quantum Hall effect [8]. Furthermore, as a consequence of the high mobilities achievable in the GaAs/AlGaAs 2DEG system, giant Faraday rotation reaching $\sim$0.8 rad was observed at modest applied magnetic fields of $\sim$100 mT. In the future, it is foreseeable that the Faraday effect arising from cyclotron motion of high-mobility charge carriers in semiconductor materials and heterostructures could be used to isolate and circulate microwave signals, in lieu of conventional bulk ferrites that rely on off-resonant Larmor procession to impart Faraday rotation. Such potential future studies are described in the following chapters.

Chapter Three

Design of a Faraday experiment for a tri-axis vector magnet cryostat at McGill

This chapter contains details on the design and methodology for upcoming Faraday rotation experiments at McGill. I designed an experiment to probe quantized rotation of microwave polarization of up to 20GHz frequency using McGill's recently commissioned low-temperature refrigerator equipped with a tri-axis vector magnet. The experiment will utilize newly grown, high-mobility GaAs semiconductor heterostructures from Dr. Loren Pfeiffer at Princeton University and a newly designed wafer apparatus to probe remaining questions about quantized Hall states via the Faraday effect.

3.1 Microwave experiment design

3.1.1 Considerations of operating frequencies

Desired operating frequencies affect the experimental parameters of waveguide experiments. Foremost, the waveguide diameter is dictated by the relationship between frequency $f = \omega/2\pi$ and $\hbar\omega_c$, where ω_c is dictated by magnetic field strength and wafer characteristics. As we have seen earlier, in the QHE, Faraday rotation angle is predicted by Fresnel analysis to become quantized as (in free space),

$$\tan(\theta_F) = i\frac{Z_0}{K}\frac{e^2}{h} = i\alpha, \tag{3.1}$$

where Z_0 is the impedance of free space and the fine structure constant, $\alpha = \gamma Z_0 e^2/h$, sets the natural scale for θ_F. The microwave frequency range (300 MHz $< f <$ 300 GHz) is particularly suitable for an experiment attempting to realize this idealized scenario because the "low-frequency" limit $\omega \ll \omega_c$, discussed in Chapter 2, can easily be achieved [4].

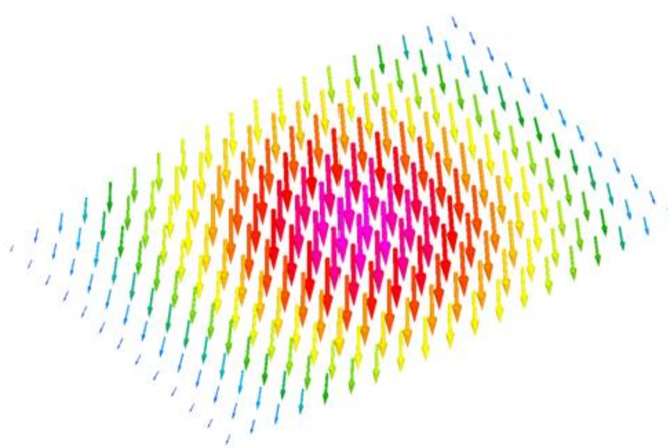

Figure 3.1 Simulation of magnetic field inside a circular waveguide. The cross sectional view in the middle of a waveguide in the YZ (or XZ) plane from QWED.eu online [52].

Due to constraints of the size cryostat magnet bore and bandwidth of the VNA, low-mid range microwave signals between 10-20 GHz was chosen for this experiment. For our experiment, we use the transverse electric (TE) modes, which means the electric field is perpendicular to the length of the waveguide and magnetic field is parallel. Specifically, our experiment utilizes the the TE_{11} mode, where half wavelength, $\lambda/2$, is supported in both x and y directions in a cross sectional plane with the waveguide.

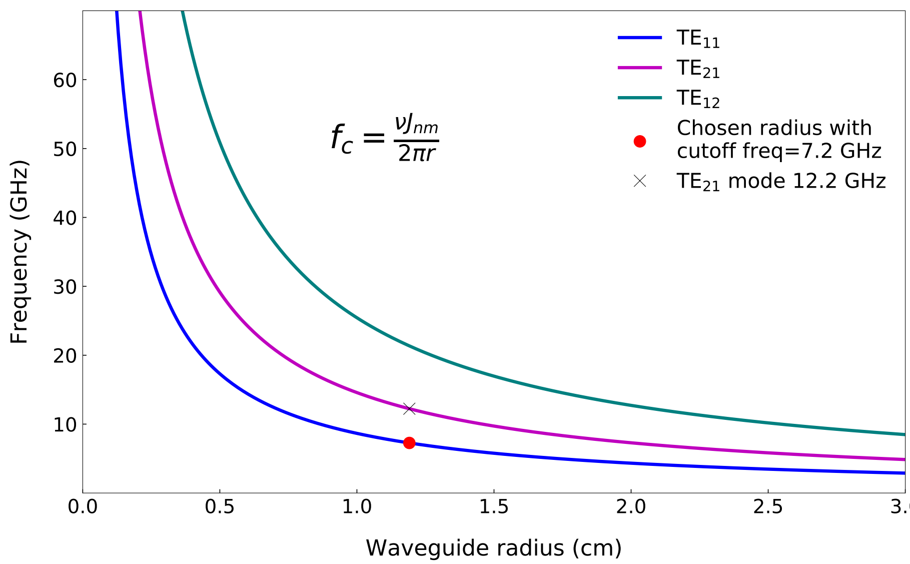

Figure 3.2 Frequency considerations for the waveguide experiment. Frequency as a function of radius is calculated using first order Bessel functions for the lowest modes. Using the TE_{11} mode for our experiment provides us with a cutoff frequency of 7.2 GHz. At 12.2 GHz, the TE_{21} mode is present, providing an upper frequency bound. To change frequencies beyond that limit, a narrower or wider waveguide could be implemented as indicated by the curves.

A simple model, assuming an infinitely long waveguide, shows the relationship between waveguide width and the electromagnetic modes at various frequencies able to pass through the waveguide cavity. We can also look at dispersion by plotting group velocity, $v_g = c\sqrt{1 - \frac{f_c^2}{f^2}}$, where c is the speed of light in a vacuum, f_c is the cutoff frequency (7.2 GHz for the TE_{11} mode in our system), and f is the frequency of the microwave signal.

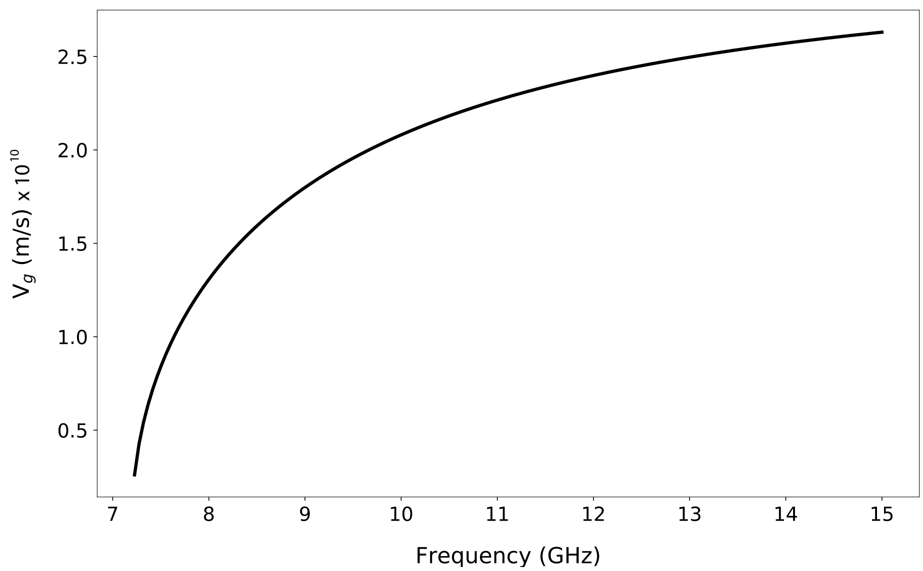

Figure 3.3 Group velocity for TE_{11} cutoff frequency as a function of microwave signal frequency.

3.1.2 Wafer configuration

The sample for this experiment is a GaAs/AlGaAs wafer grown using molecular bean epitaxy (MBE) by Loren Pfeiffer at Princeton University. These possess some of the highest electron mobilities and are made ∼0.5 mm thick in 2" round disks. GervaisLab receives the large middle portion of the circular wafers, which generally possess the best qualities, along with a data sheet including estimates of electron density and mobility (see sample wafer in Appendix D). However, the 2" disks do possess heterogeneous electron density and mobility. Therefore, the regions of the wafers that we receive must be tested for density and mobility as described in Chapter 1 Section 2. This must be done before the wafer is mounted in the waveguide to measure Faraday rotation.

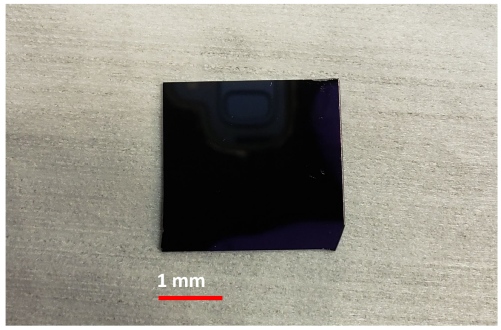

Figure 3.4 Wafer (black) from Dr. Loren Pfeiffer (P7.25.19.1). This wafer was cut into a 3 × 3 mm square to test mobility and carrier density (see Appendix A).

The wafer will be held in the waveguide by a mechanical piece acting as an iris inside the waveguide. From here, the wafer itself can be thermalized to the refrigerator via a silver cable from the wafer holder directly attached to the mixing chamber plate. The wafer holder will be made of two rectangular pieces of sapphire with holes for screws. Gold deposited on the sapphire will create the iris effect as the copper apparatus did previously (Chapter 2). The added benefit of this gold-sapphire apparatus is that any pattern of gold can be deposited onto the sapphire with high precision on the scale of tens of nanometers using clean room fabrication methods similar to those in Chapter 1. The sapphire wafer holder could also be equipped with gold lines acting as flip-chipped ohmic contacts in order to perform DC measurements on the 2DEG simultaneous to measuring microwave Faraday rotation. Additionally, sapphire is not magnetically susceptible and the gold coating offers a thermal connection between the silver-coated waveguide sections and the wafer. An additional gold wire will be attached to one of the screws in the wafer holder apparatus and to the refrigerator creating a second thermal link.

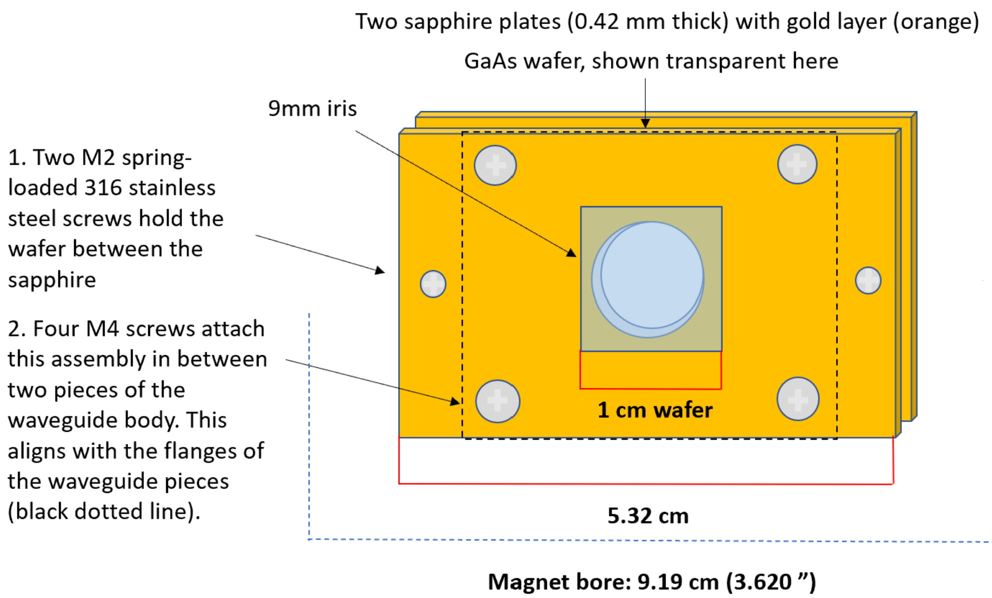

Figure 3.5 Apparatus to hold the wafer inside the waveguide. The wafer, portrayed transparently here, is placed between two gold-coated sapphire plates held by two spring-loaded screws (gray). Four holes in both plates (white) allow the closed assembly to be placed in between the circular sections of the waveguide (Fig. 3.6 right). Sapphire is used to reduce interference with the microwaves passing through the transparent iris, while providing mechanical support for the wafer. Gold deposited onto the sapphire thermally connects the wafer to the refrigerator via the waveguide body.

3.1.3 Waveguide design

Similar to the Sherbrooke experiment, our waveguide is comprised of five pieces fabricated by Cernex Wave, with certain custom specifications (see Appendix C). Most basically, the waveguide experiment is designed to support microwave signals passing through the 2DEG. The goal is to provide an environment which has little or calculable effect on the microwaves, such that we can extract and analyse the behaviour of the 2DEG alone.

Since Faraday rotation depends on magnetic field, it is important to utilize materials, other than the semiconducting heterostructure under study, that are not susceptible to mag-

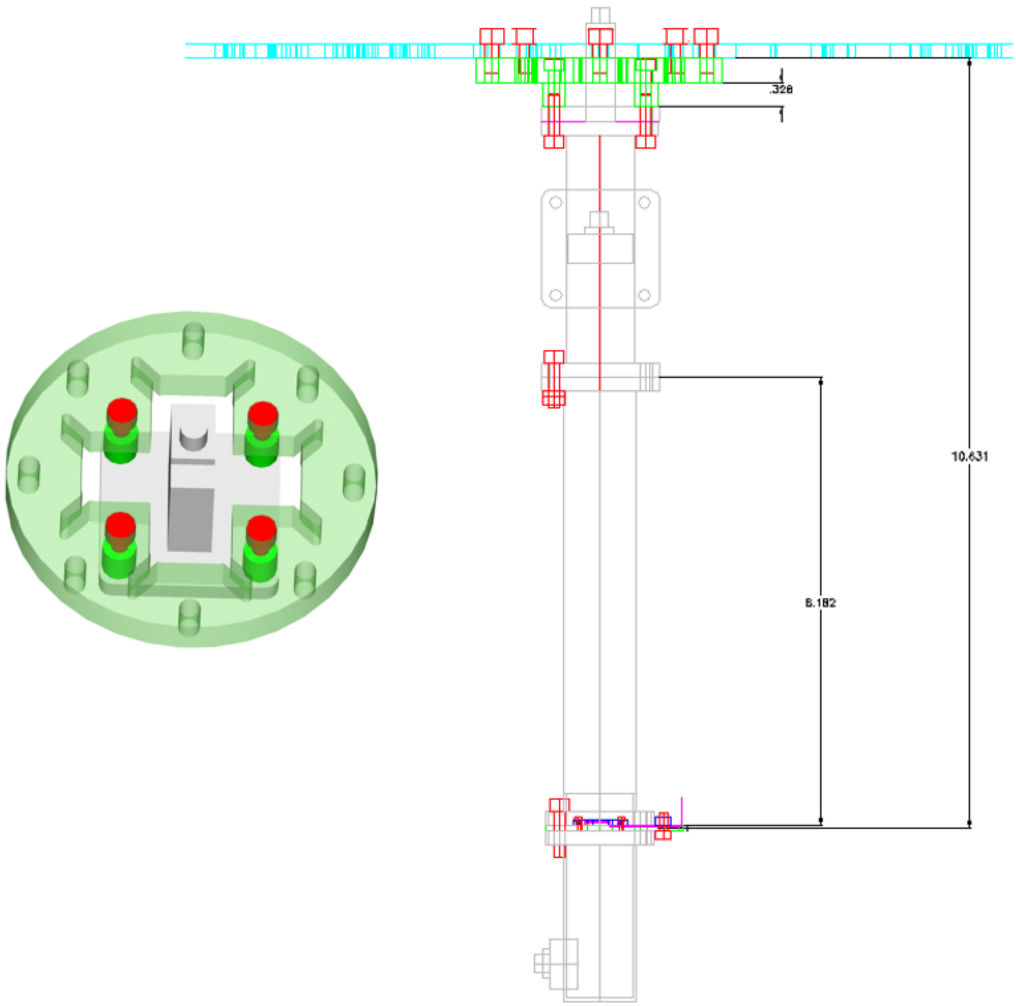

Figure 3.6 AutoCAD design for the waveguide and placement in the Oxford Triton refrigerator. Left: 3D image of the top of the piece that holds the waveguide to the MC plate. Four screws attach the waveguide body to the piece, which is then held on to the MC plate using the eight threaded holes seen around the circumference. Notches are cut in radially to reduce eddy currents circling the piece. **Right:** The waveguide is fixed to the mixing chamber (MC) plate (blue) by a gold-plated copper apparatus (green, also depicted in 3D Right) and sits surrounded by the magnet (not pictured here). The microwave signal enters the waveguide via an electric dipole at the bottom, is transmitted past the wafer, up the length of the waveguide and is split by the orthomode transducer and passed through two orthogonal electric dipoles into coaxial cables back out of the refrigerator.

netisation and to some extent, not overly sensitive to eddy currents. This is because currents are induced in metal in the presence of a varying magnetic field, not only inducing a secondary electromagnetic field but also creating a thermal heat leak that is detrimental to low temperature experiments. Gold and silver are not magnetically susceptible but are costly and highly malleable. Brass is a strong, low-cost alloy made of copper and zinc, as well as other trace elements, and is only slightly magnetically susceptible due to trace iron. The waveguide body is made of silver-plated brass, utilizing silver for its high thermal conductivity to help lower the 2DEG's temperature towards that of the refrigerator.

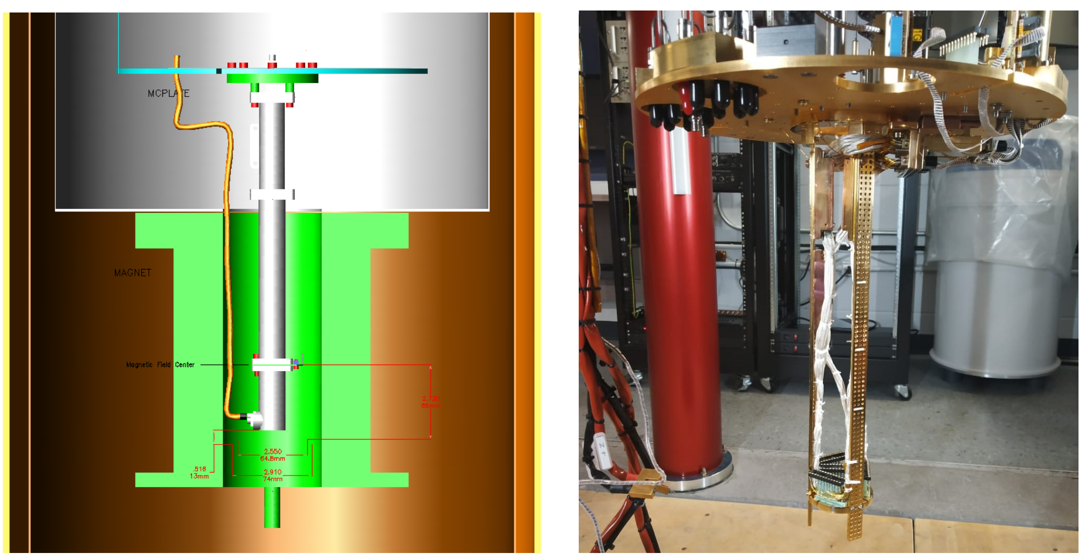

Figure 3.7 Oxford Triton refrigerator tail. The waveguide assembly is attached to the MC plate housed inside the magnet bore. **Left:** 3D AutoCAD drawing with magnet in enclosed refrigerator. **Right:** The open refrigerator with MC plate shown without the waveguide.

Another important factor in measuring Faraday rotation of microwaves through the 2DEG is the ability to provide a conducive environment for maintaining the electron gas itself. Aside from the MBE process of creating a wafer with quantum wells to host a 2DEG, the semiconductor must be at sufficiently low temperatures for the electron gas to be present during experimentation by creating thermal connections between the wafer and the cryostat. Since the lowest plate, known as the mixing chambre (MC), is by design the coolest region, the waveguide assembly is attached to this gold-coated plate. The tail fits inside the region of the strongest magnetic field within the magnet bore. The gold plating on the attachment piece and on the MC plate thermally links the waveguide to the refrigerator. To avoid eddy currents induced in-plane of the copper apparatus by the perpendicular magnetic field via Faraday's law, notches or holes are cut in to the plate to disrupt the currents (Fig 3.6 left).

3.2 Laboratory configuration

3.2.1 VNA Data Configuration

Microwave signals will be sent from and returned to the two-port Rohde & Schwarz ZVM vector network analyzer (VNA) mounted on a rack beside the refrigerator. The VNA is controlled entirely by a user-interfaced software, LabGUI, which was created by previous GervaisLab students and maintained by current students. A new driver for the VNA was written for LabGUI to read and interface with the machine. The driver contains basic read and write functions as per the VNA's protocols, which are packaged and transmitted by LabGUI via General Purpose Interface Bus (GPIB).

3.2.2 Experimental circuit

The waveguide receives the microwave signals via semi-rigid coaxial cables that run to and from the high frequency coaxial cables of the refrigerator. Cables both internal and external

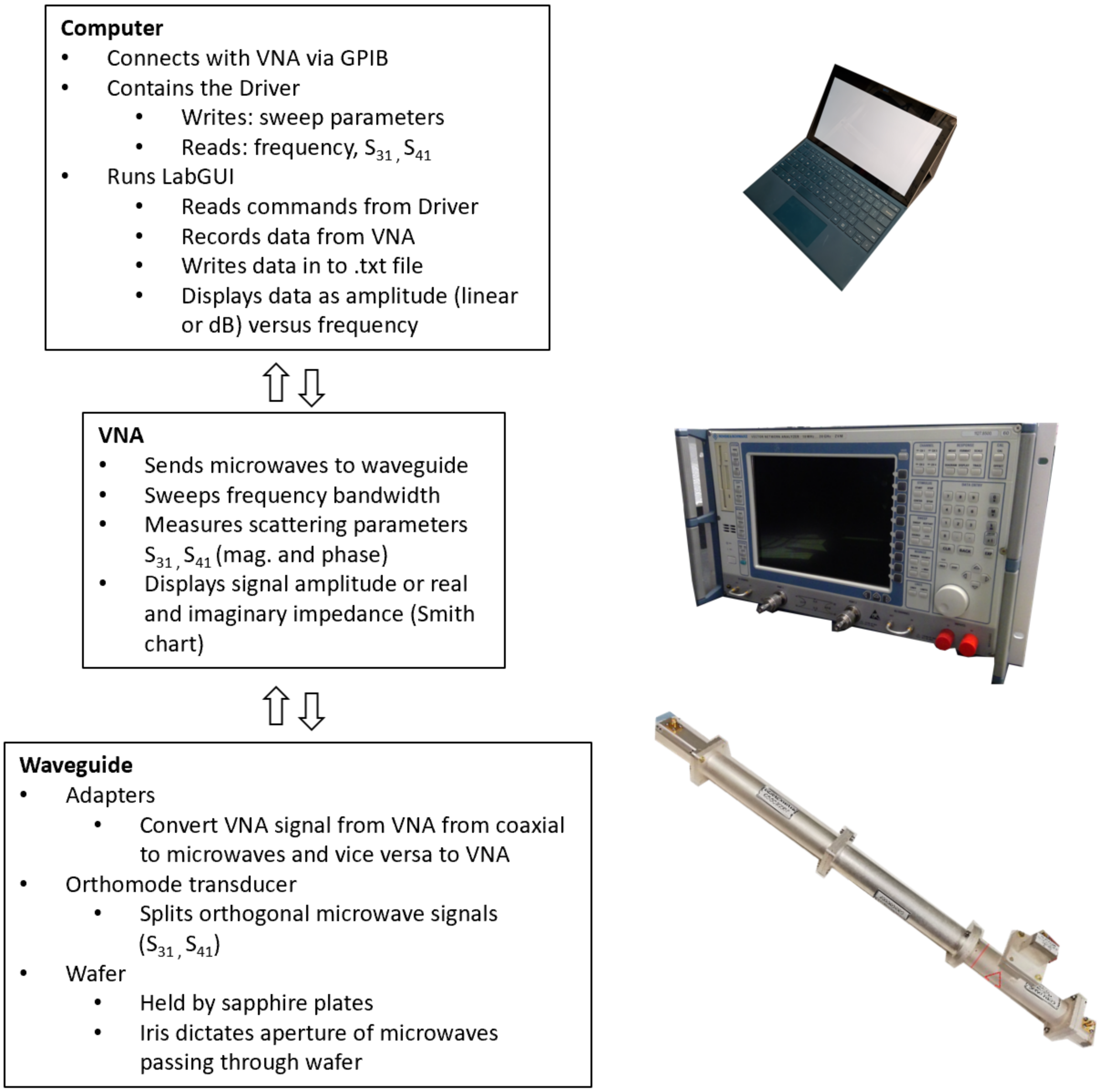

Figure 3.8 Storyboard of the experiment. The computer software send commands to the VNA such that signals are transmitted to and measured from the waveguide experiment. Data is collected on the computer and housed locally and in the cloud.

to the refrigerator are fitted with 2.92 mm ends and adapters with 50 ohm impedance, which support frequencies up to 40 GHz. The VNA is fitted with 3.50 mm adapters, therefore one

3.50 mm to 2.92 mm converter is employed. The cables that sit inside the refrigerator are thermally connected to each plate (listed by temperature in Fig. 3.9).

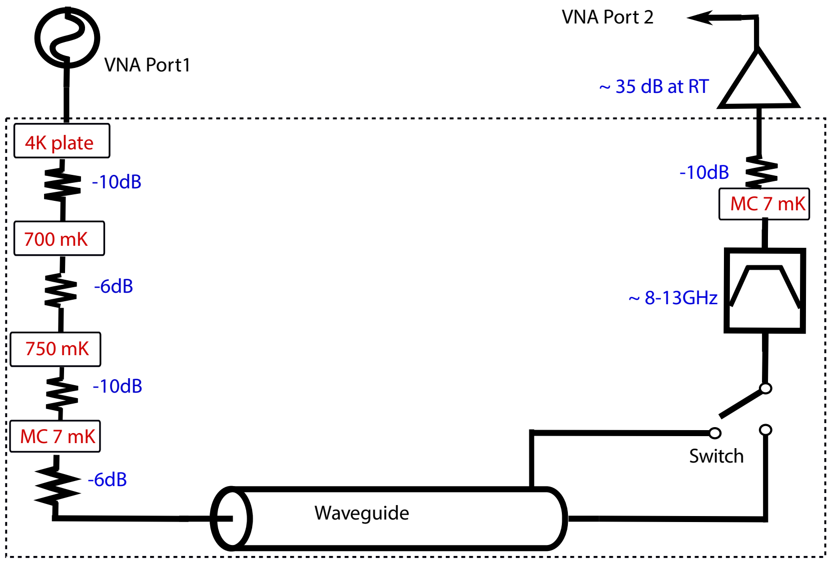

Figure 3.9 Filters and attenuators circuit for microwave signals to and from VNA. Filters are used to remove potential noise outside the desired microwave bandwidth chosen for the experiment. Attenuators help mitigate heating from the incoming signals. Each device's location is denoted in between the various refrigerator plates and the dotted box delineates what is inside and outside of the refrigerator.

Chapter Four

Conclusion

We have developed a theoretical and experimental road map for further experiments in quantized Faraday rotation, in part inspired by lessons learned from previous experiments in the QHE. We have performed DC experiments in the QHE with Van der Pauw and Hall geometries which, with high enough mobility wafers, display integer and fractional states via edge currents. We have examined preliminary measurements of quantized and giant Faraday rotation and discussed future microwave waveguide experiments. Certain DC measurement techniques and device configurations could lend themselves to cutting edge Faraday rotation manipulation. Paired with even higher mobility samples, robust measurements using microwave signals could illuminate elusive many-body FQHE states, as well as offer applications for communication technologies. Our future experimental goals fall in to two categories: measuring giant Faraday rotation at room temperature and demonstrating fractionally-quantized Faraday rotation at low-temperatures–a first.

4.1 Future experiments at room temperature

A major application for Faraday rotation could be in the replacement of conventional bulk ferrites in microwave non-reciprocal devices such as circulators and isolators. Observing giant Faraday rotation at room temperature, around or above $\pi/2$, could pave the way for more robust, competitive technologies for microwave engineering. There are two qualities of materials which might support large or giant Faraday rotation at room temperature: high mobility and high spin-orbit coupling materials.

4.1.1 High mobility materials

Chapter 1 presented the importance of high charge carrier mobility in quantum Hall physics, whereby electrons are afforded long, collision-free paths within their low-dimensional environments. Past experiments in quantized Faraday rotation have used wafers with a 2DEG of $\sim 1{\times}10^6$ cm^2 V^{-1} s^{-1} mobility [4]. However, the highest 2DEG mobilities in condensed matter are over an order of magnitude higher than what was used in our published study, at 35×10^6 cm^{2}V^{-1}s^{-1}, leaving room for improvement in our experiments with quieter electron systems [18]. All mobilities and resistance values presented in Chapter 1 and 2 are quoted at cryogenic temperatures, below 4K. At such temperatures, electrons have the ability to sink into a 2D quantum well. At room temperature, 2DEGs in GaAs semiconductors do not exist and wafer resistance can increase by four orders of magnitude. There are other materials which possess moderately high mobilities at room temperatures, which could likely be high enough to support giant Faraday rotation. Graphene is known to have room temperature mobilities exceeding 1.4×10^4 cm^2 V^{-1} s^{-1} [53] and has been suggested as a candidate for microwave technologies [54]. Additionally, bismuth wires have been shown to support mobilities of up to 2.45×10^4 cm^2 V^{-1} s^{-1} [55], where high mobility is thought to come from the edges as opposed to the bulk, which has lower carrier mobility, around 1×10^4 cm^2 V^{-1} s^{-1} [56].

4.1.2 High spin-orbit materials

High spin-orbit materials are known to also support quantized energy states [57], which might be more robust at room temperatures. Quantized spin-orbit states are predicated on the current created by a linearly changing magnetic field, which induces a net change in spin inside a region of a material. This quantum spin conductivity could be utilized for QHE measurements. One way to measure this spin current is via spin accumulation at the edges. Materials with large diamagnetic susceptibility and large band gaps, such as bismuth [57] and graphene, or graphite in 2D [58], are currently thought to support this. Measuring spin-orbit quantization using microwaves or other high frequency signals in a waveguide at room temperature would be a first. InAs/AlSb (type I) and InAs/GaSb/AlSb (type III) quantum wells also provide promising materials for hosting giant microwave Faraday rotation at room temperature with mobilities between 3 to 6×10^4 cm^2 V^{-1} s^{-1} [59, 60]. Type I quantum wells offer high mobility at room temperature . Type III wells can be tuned between topologically trivial and non-trivial states. Using these materials at room temperature could provide the largest Faraday rotation yet observed, and perhaps with no magnetic field at all, and offer direct applications for communications technologies.

4.2 Fractional quantum Faraday effect

Whereas nearly all fractional quantum Hall states mentioned in past work were first observed using edge current DC measurements, this thesis paves the way forward to study the many-body FQHE via contactless Faraday rotation. The first step towards this goal will be to conduct the waveguide experiment presented in Chapter 3 with higher mobility wafers, *i.e.* higher than our study discussed in Chapter 2. Currently, we have access to 2DEGs with mobilities as high as 30×10^6 cm^2 V^{-1} s^{-1}, which is thirty times higher than that of our past experiments. Observing fractionally-quantized Faraday rotation will require improvements in 2DEG cooling preparation, signal purity and and thermalization of the electrons to unleash the many-body interactions in the 2D bulk.

It could be that, whereas our observed integer Faraday quantization is quite pronounced (see Fig. 2.6), the scale of the fractional plateaus would be small such that a quieter system with less reflection from the waveguide and/or iris apparatuses would be required. Hence, future experiments might benefit from a square waveguide and sufficiently large wafer such that any affects from the apparatus holding the wafer are eliminated.

Ultimately, many questions about the QHE also remain, especially for fractional states. Quantized Faraday rotation offer promising insights into the rich world of quantum phases potentially leading to new insights for 21st century physics, engineering, and beyond.

REFERENCES

1. Von Klitzing, K. *Rev. of Mod. Phys.* **58,** 519 (1986).
2. Dean, C. R. *A Study of the Fractional Quantum Hall Energy Gap at Half Filling* (2008).
3. Hall, E. H. *American Journal of Mathematics* **2,** 287 (1879).
4. Suresh, V., Pinsolle, E., Lupien, C., Martz-Oberlander, T. J., Lilly, M. P., Reno, J. L., Gervais, G., Szkopek, T. & Reulet, B. *Phys. Rev. B* **102,** 085302 (2020).
5. Von Klitzing, K., Dorda, G. & Pepper, M. *Phys. Rev. Lett* **45,** 494 (1980).
6. *National Institute of Standards and Technology (NIST)* <https://www.physics.nist.gov/cgi-bin/cuu/Value?rk> (Accessed Aug. 2020).
7. Cage, M. E., Dziuba, R. F. & Field, B. F. *IEEE Trans. on Instr. and Meas.* **34,** 301 (1985).
8. Tsui, D. C., Stormer, H. L. & Gossard, A. C. *Phys. Rev. Lett* **48,** 1559 (1982).
9. Haldane, F. D. M. *Phys. Rev. Lett.* **67,** 937 (1991).
10. Moore, G. & Read, N. *Nucl. Phys. B* **360,** 362 (1991).
11. Willett, R. L., Pfeiffer, L. N. & West, K. W. *PNAS* **106,** 8853 (2008).
12. Pan, W., Xia, J.-S., Shvarts, V., Adams, D. E., Stormer, H. L., Tsui, D. C., Pfeiffer, L. N., Baldwin, K. W. & West, K. W. *Phys. Rev. Lett.* **83,** 3530 (1999).
13. Pan, W., Stormer, H. L., Tsui, D. C., Pfeiffer, L. N., Baldwin, K. W. & West, K. W. *Phys. Rev. Lett.* **90,** 016801 (2003).
14. Rodríguez, E., Martín, E. & González, E. *Ingeniería e Investigación* **31,** 144 (2011).
15. Dingle, R., Störmer, H., Gossard, A. & Wiegmann, W. *Appl. Phys. Lett.* **33,** 665 (1978).
16. Prange, R. & Girvin, S. *The Quantum Hall Effect* (Springer-Verlag, 1987).

17. Datta, S. *Electron Transport in Mesoscopic Systems* (Cambridge University Press, 1995).

18. Umansky, V., Heiblum, M., Levinson, Y., Smet, J., Nübler, J. & Dolev, M. *Journ. of Cryst. Grow.* **311,** 1658 (2009).

19. Schmidt, B. A. *Specific Heat in the Fractional Quantum Hall Regime* (2019).

20. Willett, R. L., Nayak, C., Shtengel, K., Pfeiffer, L. N. & West, K. W. *Phys. Rev. Lett.* **111,** 186401.

21. Neder, I., Heiblum, M., Levinson, Y., Mahalu, D. & Umansky, V. *Phys. Rev. Lett.* **96,** 016804 (2006).

22. Ji, Y., Chung, Y., Sprinzak, D., Heiblum, M., Mahalu, D. & Shtrikman, H. *Nature* **422,** 415 (2003).

23. Willett, R. L., Pfeiffer, L. N. & West, K. W. *PNAS* **106,** 8853 (2009).

24. Ofek, N., Bid, A., Heiblum, M., Stern, A., Umansky, V. & Mahalu, D. *PNAS* **107,** 5276 (2010).

25. De C. Chamon, C., Freed, D. E., Kivelson, S. A., Sondhi, S. L. & Wen, X. G. *Phys. Rev. B* **55,** 2331 (1997).

26. Bennaceur, K., Schmidt, B. A., Gaucher, S., Laroche, D., Lilly, M. P., Reno, J. L., West, K. W., Pfeiffer, L. N. & Gervais, G. *Scientific Reports* **5,** 13494 (2015).

27. Beukman, A. J. A., Qu, F., West, K. W., Pfeiffer, L. N. & Kouwenhoven, L. P. *Nano Lett.* **15,** 6883 (2015).

28. Gaucher, S. *Flip-Chip Fabry-Perot Electron Interferometer* (2015).

29. Groth, D. *PC Chop Shop: Tricked Out Guide to PC Modding* (SYBEX Inc., 2005).

30. Volkov, V. A. & Mikhailov, S. A. *JTEP lett.* **41,** 476 (1985).

31. Szkopek, T. *IEEE Journ. of Quant. Elec.* **47,** 500 (2011).

32. Faraday, M. *Philo. Trans. R. Soc. London* **136** (1846).

33. Froman, D. K. *Phys. Rev.* **41,** 693 (1932).

34. Smith, F. G. *Nature* **220,** 891 (1968).

35. Skulason, H. S., Sounas, D. L., Mahvash, F., Francoeur, S., Siaj, M., Caloz, C. & Szkopek, T. *Appl. Phys. Lett.* **107** (2015).

36. Li, Y. Q., Steuerman, D. W., Berezovsky, J., Seferos D. S .and Bazan, G. C. & Awschalom, D. D. *Appl. Phys. Lett.* **88,** 33 (2006).

37. Hu, C. Y., Young, A., O'Brien, J. L., Munro, W. J. & Rarity, J. G. *Phys. Rev. B* **78,** 085307 (2008).

38. Crassee, I., Levallois, J., Walter, A. L., Ostler, M., Bostwick, A., Rotenberg, E., Seyller, T., Van Der Marel, D. & Kuzmenko, A. B. *Nat. Phys.* **7,** 48 (2011).

39. Volkov, V. A., Galchenkov, D. V., Galchenkov, L. A., Grodenskii, I. M., Matov, O. R., Mikhailov, S. A., Senichkin, A. P. & Starostin, K. V. *JTEP lett.* **43,** 255 (1986).

40. Sounas, D. L., Skulason, H. S., Nguyen, H. V., Guermoune, A., Siaj, M., Szkopek, T. & Caloz, C. *Appl. Phys. Lett.* **102,** 191901 (2013).

41. Mittleman, D. M., Cunningham, J., Nuss, M. C. & Geva, M. *Appl. Phys. Lett.* **71,** 16 (1997).

42. Ikebe, Y., Morimoto, T., Masutomi, R., Okamoto, T., Aoki, H. & Shimano, R. *Phys. Rev. Lett.* **104,** 256802 (2010).

43. Shimano, R., Yumoto, G., Yoo, J. Y., Matsunaga, R., Tanabe, S., Hibino, H., Morimoto, T. & Aoki, H. *Nat. Commun.* **4,** 1 (2013).

44. Wu, L., Salehi, M., Koirala, N., Moon, J., Oh, S. & Armitage, N. P. *Science* **354,** 1124 (2016).

45. Shuvaev, A, Dziom, V, Kvon, Z. D., Mikhailov, N. N. & Pimenov, A. *Phys. Rev. Lett.* **117,** 117401 (2016).

46. Dziom, V., Shuvaev, A., Pimenov, A., Astakhov, G. V., Ames, C., Bendias, K., Böttcher, J., Tkachov, G., Hankiewicz, E. M., Brüne, C., Buhmann, H. & Molenkamp, L. W. *Nat. Commun.* **8,** 1 (2017).

47. Bethe, H. A. *Phys. Rev.* **66,** 163 (1944).

48. Novoselov, K. S., McCann, E., Morozov, S. V., Fal'ko, V. I., Katsnelson, M. I., Zeitler, U., Jiang, D., Schedin, F. & Geim, A. K. *Nat. Phys.* **2,** 177 (2006).

49. Xiao, D., Chang, M.-C. & Niu, Q. *Rev. Mod. Phys.* **82,** 1959 (2010).

50. König, M., Wiedmann, S., Brüne, C., Roth, A., Buhmann, H., Molenkamp, L. W, Qi, X.-L. & Zhang, S.-C. *Science* **318,** 766 (2007).

51. Chang, C.-Z, Zhang, J., Feng, X., Shen, J., Zhang, Z., Guo, M., Li, K., Ou, Y., Wei, P., Wang, L.-L., Ji, Z.-Q., Feng, Y., Ji, S., Chen, X., Jia, J., Dai, X., Fang, Z., Zhang, S.-C., He, K., Wang, Y., Lu, L., Ma, X.-C. & Xue, Q.-K. *Science* **340,** 167 (2013).

52. QW-Ed. *QW-Modeller* <https://www.qwed.eu/QuickWave/qwmodeller_help/microwave_course/3_2_mode_te11.htm> (Accessed Aug. 2020).

53. Kim, M. S., Kim, M., Son, S., Cho, S. Y., Lee, S., Won, D. K., Ryu, J., Bae, I., Kim, H. M. & Kim, K. B. *ACS Appl. Mater. Interfaces* **12,** 30932 (2020).

54. Sounas, D. L. & Caloz, C. *IEEE Trans. on Microw. Theor. and Tech.* **60,** 901 (2012).

55. Hasegawa, Y., Murata, M., Nakamura, D., Komine, T., Taguchi, T. & Nakamura, S. *Journal of Applied Physics* **105,** 103715 (2009).

56. Arisaka, T., Otsuka, M. & Hasegawa, Y. *Journal of Applied Physics* **123,** 235107 (2018).

57. Murakami, S. *Phys. Rev. Lett.* (2006).

58. Wang, D., Che, S., Cao, G., Lyu, R., Watanabe, K., Taniguchi, T., Lau, C. N. & Bockrath, M. *Nano. Lett.* **19,** 3 (2019).

59. Bennett, B. R., Magno, R., Boos, J. B., Kruppa, W. & Ancona, M. G. *Solid-State Elec.* **49,** 1875 (2005).

60. Lehner, C. A., Tschirky, T., Ihn, T., Dietsche, W., Keller, J., Fält, S. & Wegscheider, W. *Phys. Rev. Materials* **2,** 054601 (2018).

APPENDIX

Appendix A

Wafer cleaving process

The following steps outline how to cleave a wafer by hand.

Materials needed:

1. non-metal tweezers (I like the static-guard plastic type seen here),
2. lint-free lab wipe (the plastic clean room type offer proper cushioning),
3. a diamond tip cutter,
4. a curved razor with handle (see images).

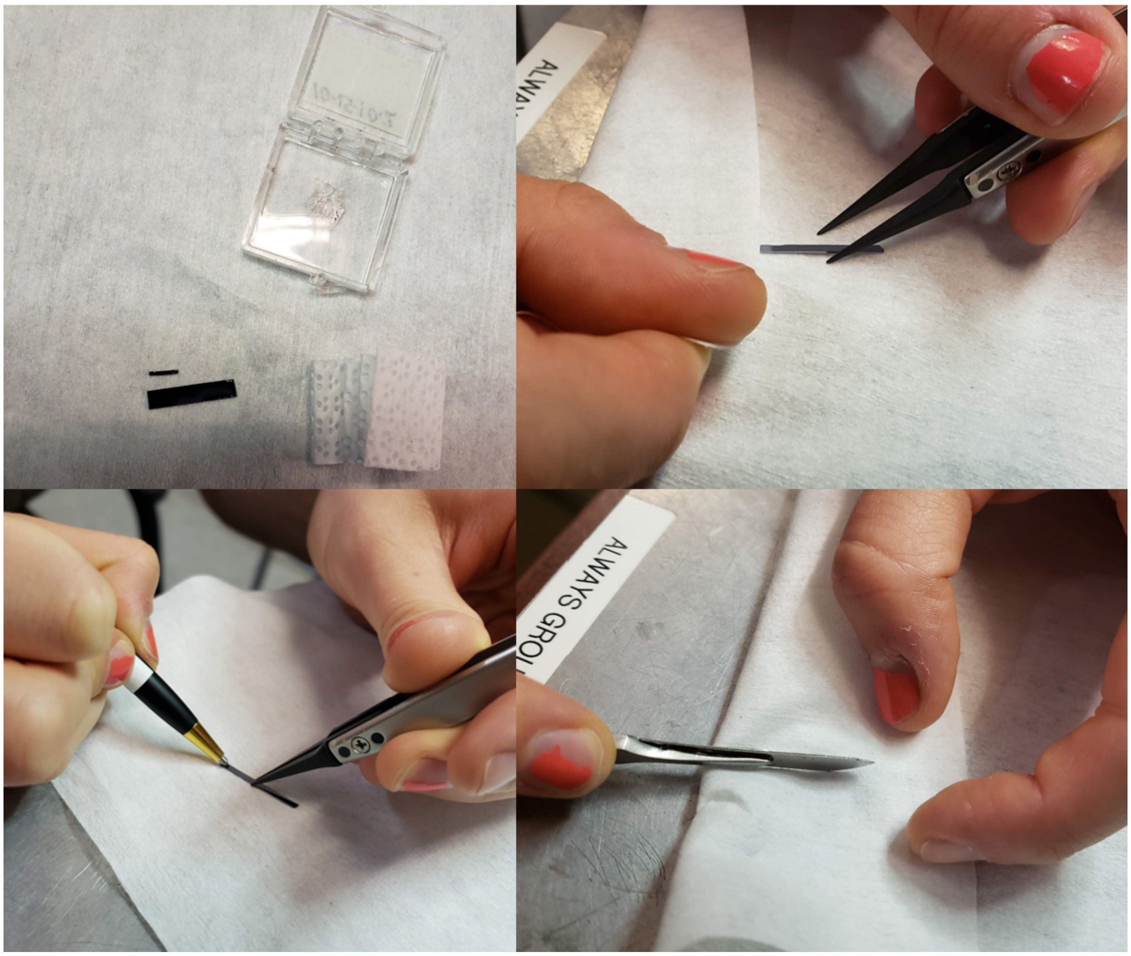

Figure A.1 Steps to cleave a wafer: left, top-bottom then right, top-bottom. Left: We start with a large rectangular GaAs wafer we want to cleave to the size of the small piece beside it. Hold the wafer face up very gently with the tweezers. With the diamond tip pen, score just the edge of the wafer at the desired width. You should use barely any pressure, just enough so that you can see a short line where you scored. **Right:** with the tweezers, flip the wafer upside down and fold some the wipe over top. Remembering where you scored the wafer, place the blade down on the cloth just below the edge of the wafer. Slowly and quite gently roll the blade upwards towards its tip. You do not have to apply pressure in any part of the process. The wafer will break along the crystal axis where you left the score.

Appendix B

Wafer cleaning recipe

The following process was used to clean wafers for mounting in flip chip devices. Always make careful note of solvent flashpoint temperatures. If you are concerned about the wafer breaking due to the mechanical stress of sonication, you can line the beaker with a clean room -grade wipe.

1. In a small beaker, sonicate the wafer in trichloroethylene (TCE) at 30^o C for 10 minutes. Note, this is a strong solvent only necessary if you suspect there is grease on the wafer,
2. Sonicate in methanol at 30^o C for 10 minutes,
3. Sonicate in isopropanol (IPA) at 50^o C for 5 minutes,
4. Spray with deionized water, careful not to drop the wafer,
5. Spray dry with nitrogen, or air, to further prevent droplet residue.

Appendix C

McGill Faraday experiment waveguide parts

Details of the parts ordered from Cernex Wave in California, USA from Chapter 3.

Qty	Item	Description
1	COT09110335-03	Orthomode Transducer: WR-90, Freq: 9-11GHz, IL: 0.3dB Max, VSWR: 1.25:1 Max; Isolation: 35dB Min, Flanges: FBP100, Copper/Silver Plating, Length: 90mm, No Paint
1	CWKC90091103F-01	Coaxial to Circular Waveguide Adapter: WR-90, 9-11GHz, VSWR: 1.25:1 Max, I.L: 0.3dB Max, Flange: FBP120, 2.92mm-F, Brass, Silver Plating, No Paint
1	CSSC9006-01	Circular WG Section: 9-11GHz, VSWR:1.1:1 Max, Flanges:FBP100 & FBP120 w/M4 threads, Cir WG Dia: 23.825mm, Length: 156mm (6.14"), Brass, Silver Plating, No Paint
2	CWK90081203F-02	Waveguide to Coaxial Adapter: WR-90, 8.2-12.4GHz, I.L: 0.3dB Max, VSWR:1.25:1 Max, Power: 20W CW, 100W Peak, Flange: UG39/U to 2.92mm-F, No Paint

Figure C.1 Details of the parts ordered from Cernex Wave.

Appendix D

Sample wafer growth sheet

A sample growth sheet for high-mobility wafer from Dr. Loren Pfeiffer at Princeton University. Each line documents a different layer deposited under vacuum in the molecular beam epitaxy (MBE) process, in chronological order from line 1 through line 340. Thickness, in the third column, is listed in Angstroms. In the wafer growth sheet shown here, the quantum well is 30 nm of GaAs with 78 nm thick AlGaAs walls on either side. The well is set back ∼195 nm from the wafer's surface. Mobility and density have been tested by the wafer grower, seen in the notes at the bottom of the sheet.

3_11_10.1 - Actual Results
Substrate: F C0541 block VII
As Temp: 291
As Set: 7.8e-6
Comments: 10 th high mobilityrun, 646C

label	relay	rate	temp	set pt
Al8	1	0.8789	1001.000	17.830
Ga7	2	2.8020	929.000	929.000

Layer#	Layer Type	Thickness	Time	Total Time	Al8	Sub (V)	Si (A)	C (A)
1	chgSi chgC As10	0.00	60.00	60.00	---	28.439	0.002	0.011
2	Ga7As10	7000.00	2498.22	2558.22	---	28.439	0.004	0.012
3	PauseAs10	0.00	3000.00	5558.22	---	28.437	0.002	0.009
4*	Al8Ga7As10	100.00	27.17	5585.38	0.239	28.441	0.001	0.011
5*	Ga7As10	30.00	10.71	5596.09	---	28.440	0.000	0.010
6* (100)	PauseAs10	0.00	15.00	5611.09	---	28.441	0.002	0.012
304	Al8Ga7As10	2500.00	679.18	11524.79	0.239	28.444	0.002	0.010
305	Al8As10	19.81	22.54	11547.33	---	28.447	0.003	0.010
306	Ga7As10	5.66	2.02	11549.35	---	28.444	0.002	0.011
307	t-644.4	0.00	10.00	11559.35	---	28.444	0.002	0.010
308	chgTemp As10	0.00	120.00	11679.35	---	0.025	0.003	0.010
309	chgTemp As10	0.00	2.00	11681.35	---	18.111	0.002	0.009
310	chgSi As10	0.00	15.00	11696.35	---	18.107	7.413	0.010
311	SiAs10	0.00	28.00	11724.35	---	18.106	7.414	0.010
312	chgSi As10	0.00	10.00	11734.35	---	18.106	0.000	0.010
313	Ga7As10	22.60	8.07	11742.41	---	18.105	0.002	0.011
314	t-441.5	0.00	10.00	11752.41	---	18.105	0.002	0.011
315	chgTemp As10	0.00	120.00	11872.41	---	32.166	0.003	0.009
316	startTempAs10	0.00	2.00	11874.41	---	28.439	0.002	0.009
317	PauseAs10	0.00	120.00	11994.41	---	28.439	0.002	0.012
318	Al8As10	19.81	22.54	12016.95	---	28.442	0.002	0.011
319	Al8Ga7As10	780.00	211.90	12228.86	0.239	28.443	0.003	0.011
320	Ga7As10	300.00	107.07	12335.92	---	28.442	0.001	0.010
321	Al8Ga7As10	780.00	211.90	12547.83	0.239	28.442	0.004	0.010
322	t-647.7	0.00	10.00	12557.83	---	28.442	0.003	0.012
323	Al8As10	19.81	22.54	12580.37	---	28.443	0.002	0.011
324	Ga7As10	5.66	2.02	12582.39	---	28.441	0.002	0.010
325	chgTemp As10	0.00	120.00	12702.39	---	0.022	0.004	0.011
326	chgTemp As10	0.00	2.00	12704.39	---	18.103	0.003	0.011
327	chgSi As10	0.00	15.00	12719.39	---	18.105	7.416	0.012
328	SiAs10	0.00	55.00	12774.39	---	18.105	7.415	0.010
329	chgSi As10	0.00	10.00	12784.39	---	18.105	0.000	0.011
330	Ga7As10	22.60	8.07	12792.45	---	18.107	0.002	0.011
331	t-449.3	0.00	10.00	12802.45	---	18.106	0.002	0.010
332	chgTemp As10	0.00	120.00	12922.45	---	31.150	0.003	0.010
333	startTempAs10	0.00	2.00	12924.45	---	28.440	0.004	0.012
334	Al8As10	19.81	22.54	12946.99	---	28.439	0.002	0.010
335	Al8Ga7As10	1000.00	271.67	13218.67	0.239	28.441	0.003	0.010
336	Ga7As10	100.00	35.69	13254.35	---	28.441	0.002	0.010
337	t-643.1	0.00	10.00	13264.35	---	28.443	0.003	0.010
338	chgTemp As10	0.00	2.00	13266.35	---	10.081	0.003	0.009
339	chgSi chgC As10	0.00	60.00	13326.35	---	10.080	0.392	0.399
340	BeepAs10	0.00	10.00	13336.35	---	10.079	0.389	0.401

total layers: 340
total time: 13336.35 sec.
total thickness: 25595.8 A.

3-11-10.1.sum.txt

SAMPLE: 3-11-10.1 STRUCTURE: 2Dx1 MEASURED: 3/12/2010 3:53 PM
POSITION: A DARK CONTACTS: ~~flats~~ Corners MANUAL CONTROL
COMMENTS:
SOURCE CURRENT: 10.0uA MAGNET CALIBRATION (G/A): 153.0 MAGNET CURRENT (A): 3.0

T	Ro	Rh	M	D
294.9	1.9401E+3	1.1255E+7	5.8014E+3	5.5529E+11
77.4	9.0279E+1	1.9030E+7	2.1079E+5	3.2844E+11
3.8	2.1321E+0	2.1622E+7	1.0141E+7	2.8906E+11

AFTER LIGHT

T	Ro	Rh	M	D
3.8	2.0817E+0	2.0932E+7	1.0055E+7	2.9858E+11

SAMPLE: 3-11-10.1 STRUCTURE: 2Dx1 MEASURED: 3/12/2010 4:09 PM
POSITION: A AFTER LIGHT CONTACTS: flats MANUAL CONTROL
COMMENTS:
SOURCE CURRENT: 10.0uA MAGNET CALIBRATION (G/A): 153.0 MAGNET CURRENT (A): 3.0

T	Ro	Rh	M	D
3.8	2.3048E+0	2.0682E+7	8.9737E+6	3.0219E+11

30.1M 2.99''

26M → 31M same piece

Figure D.1 Sample growth sheet from Dr. Loren Pfeiffer.